



***Chemical patterns of erupting silicic magmas and
their influence on the amount of degassing during
ascent***

Alain BURGISSER¹
burgisse@cnrs-orleans.fr

Bruno SCAILLET
bscaille@cnrs-orleans.fr

HARSHVARDHAN

ISTO-CNRS, 1a rue de la Férollerie, 45071 Orléans cedex 2, France

¹Corresponding author

Word count: Abstract 210, Main text 6550

3 Tables, 13 Figures

For submission to: JGR

Abstract

We present a chemical model of magma degassing based on nine volatile species part of S-O-H-C-Fe-bearing rhyolitic melts. It is based on equilibrium, closed-system degassing, and does not take in account the crystallization of mineral phases. For given initial conditions at depth, the model calculates the gas composition as pressure decreases, as well as physical variables controlling conduit flow. We conducted a parametric study of degassing by varying initial conditions at depth within the range typical of arc magmas and characterizing the chemical evolution of the volatile components during the ascent to the surface. The resulting complex patterns of chemical changes are controlled by four groups of interrelated parameters: 1) redox state, $f \text{H}_2$, and $\text{H}_2\text{S}/\text{SO}_2$ ratio in the gas phase, 2) gas amount, 3) melt water content and $f \text{H}_2\text{O}$, and 4) relative melt sulfur content, $f \text{CO}_2$, and C/S ratio in the gas phase. The others degrees of freedom (temperature, initial pressure, and melt iron content) alter the amplitude of the chemical fluctuations during ascent, but do not change the general degassing patterns. When degassing starts at depth, volatile chemistry has little effect on the amount of degassing as measured by the evolution of porosity. Magma expansion at shallow levels, however, can be greatly affected by degassing chemistry.

1 **Introduction**

2 Monitoring of gas plumes is a major tool to mitigate volcanic eruptions (e.g.,
3 Young et al. 1993). Volcanologists have long noted that not only the chemical
4 composition of the gases emitted at the vent during eruptions varies widely from
5 volcano to volcano, but also that it often changes during the course of a single
6 eruption (Symonds et. al, 1994). In parallel, recent progresses in experimental
7 petrology and thermodynamic modeling have made possible to calculate the gas
8 composition that coexists with a given magma at depth (e.g., Ghiorso and Sack, 1995;
9 Papale, 1999; Moretti et al., 2003; Scaillet & Pichavant, 2003; Moretti and Ottonello,
10 2005; Papale et al., 2006). It has recently been shown that chemical modeling of
11 degassing has the potential to bridge the apparent discrepancy between gas
12 compositions calculated at depth and measured at the surface, as it shows that similar
13 initial conditions at depth can lead to very different chemical evolution during ascent.
14 Modeling of magmatic degassing (e.g., Papale and Polacci, 1999; Newman and
15 Lowenstern, 2002; Moretti and Papale, 2004; Papale, 2005; Aiuppa et al., 2007;
16 Burgisser and Scaillet, 2007) has largely benefited from the recent expansion of
17 carefully controlled experimental databases, and their outputs show such complex
18 degassing patterns that it is impossible to predict the gas composition at vent without
19 actually performing the full calculation.

20 In this work, we use such a degassing model to map out the evolution of natural,
21 volatile-bearing rhyolitic melts in order to asses the effects of intensive parameters on
22 the chemical evolution of the magmas during their ascent to the surface. We build on
23 previous work, which focused on O-H and S-O-H-Fe systems (Burgisser and Scaillet,
24 2007), by extending our chemical model of magma ascent to nine volatile species:
25 H₂O, H₂, O₂, SO₂, H₂S, S₂, CO₂, CO, and CH₄. These species comprise >99 mole% of

26 the volatiles commonly measured in arc volcanoes (Delmelle and Stix, 2000). The
27 role of dissolved iron and the possibility of precipitating graphite in the gas phase are
28 also taken in account. Altogether these species belong to the S-O-H-C-Fe system,
29 which controls the redox state of the ascending magma we model.

30 We assume degassing occurs at equilibrium and in a closed system, which allows
31 us to calculate gas composition by mass balance using a combination of chemical
32 reactions in the gas phase and solubility laws. This model explores a research venue
33 by which the conserved quantities during decompression are the total amount of
34 atomic C, S, O, and H. As a result, the redox state of the ascending magma is
35 calculated by the model as pressure decreases, relaxing the constraint of imposing a
36 given redox buffer, thus inaugurating an approach complementary to that of, e.g.,
37 Moretti and Papale (2004). One shortcoming is that species activities in the melt are
38 not calculated, which prevents our model to solve for the crystallization of mineral
39 phases. In particular, we cannot consider the role of iron in crystals as redox buffer,
40 which restricts us to cases where either magma ascent is fast enough to avoid
41 extensive crystallization, or melt chemistry does not allow Fe- or S-bearing crystals to
42 precipitate. On the other hand, our assumption of equilibrium implies that the model
43 does not capture the diffusion-controlled chemical evolution occurring in the near-
44 fragmentation region of the Plinian regime (Gardner et al., 1999).

45 For given conditions at depth, the model calculates the gas composition as
46 pressure decreases. After laying out the model inner workings, we present its
47 calibration against experimental data and review key assumptions. We then conduct a
48 parametric study of degassing by varying initial conditions within the range of values
49 commonly found in arc magmas, so as to tally the degassing behavior of these natural

50 systems. We finally explore how the chemistry of degassing influences the
51 development of porosity during ascent.

52 **Chemical model of the C-S-O-H-Fe system**

53 The chemistry formulation is based on that of Burgisser & Scaillet (2007) and
54 Clemente et al. (2004). The gas phase is composed of $n=9$ species, each with a molar
55 fraction m_i :

$$56 \quad \sum_{i=1}^n m_i = 1 \quad (1)$$

57 Conversion between molar fraction and weight fraction is:

$$58 \quad x_i = \frac{m_i M_i}{\sum_j m_j M_j} \quad (2)$$

59 where M_i are molecular weights of each species. The total weight fraction of each
60 species (w_{Ti}) is the sum of its exsolved part and its dissolved part:

$$61 \quad w_{Ti} = w_{gT} x_i + a_i (f_i)^{b_i} (1 - w_{gT}) \quad (3)$$

62 where w_{gT} is total gas weight fraction, a_i and b_i are solubility constants determined
63 experimentally (Table 1), and f_i is species fugacity. Equation (3) assumes Henrian-like
64 behavior of the volatile species, with a temperature dependence on solubility for H₂O,
65 H₂S, and CO₂. As shown in the next section, the total gas weight fraction in the
66 second term on the right-hand-side of Equ. (3) can be neglected so as to simplify the
67 numerical resolution:

$$68 \quad w_{Ti} = w_{gT} x_i + a_i (f_i)^{b_i} \quad (3a)$$

69 We assume the gas phase is an ideal mixture of non-ideal gases, which yields the
70 following expression for fugacities:

$$71 \quad f_i = \gamma_i m_i P \quad (4)$$

72 where P is total pressure, and coefficients γ_i are calculated at each pressure step
 73 following Holland & Powell (1991) for H_2O , Shaw & Wones (1964) for H_2 , and Shi
 74 and Saxena (1992) for the other species. Using (2) and (4), (3a) can be written as:

$$75 \quad w_{Ti} = w_{gT} \frac{m_i M_i}{\sum m_j M_j} + a_i (\gamma_i m_i P)^{b_i} \quad (5)$$

76 The gas phase is composed of 9 species that are in equilibrium at all times:

$$77 \quad K_1 = (f H_2O)(f H_2)^{-1}(f O_2)^{-1/2} \quad (6)$$

$$78 \quad K_2 = (f SO_2)(f S_2)^{-1/2}(f O_2)^{-1} \quad (7)$$

$$79 \quad K_3 = (f H_2S)(f O_2)^{1/2}(f S_2)^{-1/2}(f H_2O)^{-1} \quad (8)$$

$$80 \quad K_4 = (f CO_2)(f CO)^{-1}(f O_2)^{-1/2} \quad (9)$$

$$81 \quad K_5 = (f CO_2)^{1/2}(f H_2O)(f CH_4)^{-1/2}(f O_2)^{-1} \quad (10)$$

82 where K_1 , K_2 , K_3 , K_4 , and K_5 are equilibrium constants following an Arrhenian
 83 dependence of the type $A+B/T$ by adopting the 1-bar temperature of interest as
 84 standard state (Ohmoto and Kerrick, 1977). The total weight percents of atomic
 85 oxygen (w_{TO}), atomic hydrogen (w_{TH}), atomic sulfur (w_{TS}), and atomic carbon (w_{TC})
 86 are given by:

$$87 \quad \frac{w_{TO}}{M_O} = \frac{w_{TH_2O}}{M_{H_2O}} + 2 \frac{w_{TO_2}}{M_{O_2}} + 2 \frac{w_{TSO_2}}{M_{SO_2}} + 2 \frac{w_{TCO_2}}{M_{CO_2}} + \frac{w_{TCO}}{M_{CO}} \quad (11)$$

$$88 \quad \frac{w_{TH}}{2M_H} = \frac{w_{TH_2O}}{M_{H_2O}} + \frac{w_{TH_2}}{M_{H_2}} + \frac{w_{TH_2S}}{M_{H_2S}} + 2 \frac{w_{TCH_4}}{M_{CH_4}} \quad (12)$$

$$89 \quad \frac{w_{TS}}{M_S} = 2 \frac{w_{TS_2}}{M_{S_2}} + \frac{w_{TH_2S}}{M_{H_2S}} + \frac{w_{TSO_2}}{M_{SO_2}} \quad (13)$$

$$90 \quad \frac{w_{TC}}{M_C} = \frac{w_{TCO}}{M_{CO}} + \frac{w_{TCO_2}}{M_{CO_2}} + \frac{w_{TCH_4}}{M_{CH_4}} \quad (14)$$

91 When there is iron dissolved in the melt, the following redox reaction occurs:



93 Instead of accounting for the activities of FeO and Fe₂O₃ dissolved into a rhyolitic
 94 melt (such as in Ghiorso and Sack., 1995; Gaillard et al., 2003a; Moretti et al., 2003;
 95 Ottonello et al., 2001; Moretti, 2005), we included the redox effects of iron into our
 96 thermodynamic model by using an empirical relationship that links, at constant
 97 temperature, the molar ratio of FeO and Fe₂O₃ to the oxygen fugacity (Kress and
 98 Carmichael, 1991):

99
$$\ln\left(\frac{m_{Fe_2O_3}}{m_{FeO}}\right) = a_{KC} \ln(fO_2) + \frac{b_{KC}}{T} + c_{KC} + \sum_k d_{KCk} m_k + f_{KC} \frac{P}{T} + h_{KC} \frac{P^2}{T} \quad (16)$$

100 where k is one of (FeO*, Al₂O₃, CaO, Na₂O, and K₂O), m_k is the total molar
 101 fraction of these species, and a_{KC} , b_{KC} , c_{KC} , d_{KCk} , f_{KC} , h_{KC} are constants given in Kress
 102 and Carmichael (1991). We calculated the redox effect of iron in the C-S-O-H system
 103 by using (16) and keeping track of the total amounts of iron (w_{TFe}), oxygen in the FeO
 104 and Fe₂O₃ form ($w_{TO(Fe)}$), and oxygen in the O₂, H₂O, SO₂, CO, and CO₂ form (w_{TO}).
 105 At each pressure step, graphite activity in the gas phase is calculated, so as to test for
 106 its precipitation.

107 **Resolution**

108 The resolution is carried out in two steps. First, P , T , w_{gT} , f_{H_2O} , f_{H_2} , f_{CO_2} , and
 109 FeO* are set at depth so that the composition of the gas phase and the total amounts of
 110 each element could be determined. Because the relation (16) contains the total molar
 111 fraction of several oxides and the mass balance of the gas phase (11-14) is in weight
 112 fraction, conversions between the two units are needed, and the total composition of
 113 the melt should also be fixed. Thus, we used the total weight fraction of 9 major
 114 oxides of a typical rhyolite (SiO₂, Al₂O₃, TiO₂, CaO, Na₂O, K₂O, MgO, MnO, and

115 P_2O_5). These initial values add up to 100%, and need to be corrected to take in
 116 account the amounts of volatiles and iron. Although the initial quantity of FeO^*
 117 (w_{TFeO^*}) is set, the initial amount of oxygen in the FeO and Fe_2O_3 form is not known
 118 and should be determined using the empirical equation (16). This renormalization
 119 imposes to first calculate the total amount of volatile elements, and the oxygen
 120 fugacity.

121 The molar composition of the gas phase can be determined by using (4) to
 122 calculate m_{H_2O} , m_{H_2} , and m_{CO_2} , by using (4, 6, 9-10) to calculate m_{O_2} , m_{CO} , m_{CH_4} , and
 123 f_{O_2} , and by using (1), (4), and (7-8) to calculate m_{SO_2} , m_{H_2S} , and m_{S_2} . Converting
 124 molar fractions to fugacities, and using the solubility laws (5) and the total gas
 125 fraction gives us the total amounts of sulfur, hydrogen, carbon and “free” oxygen w_{TO} .

126 Now, the initial quantities of the 9 major oxides can be normalized so that the 9
 127 oxides, plus the volatile elements (w_{TO} , w_{TS} , w_{TH} , and w_{TC}), plus the total iron (w_{TFeO^*})
 128 add up to 100%. Then, the total molar fraction of FeO^* , Al_2O_3 , CaO , Na_2O , and K_2O
 129 are calculated using:

$$130 \quad m_i = \frac{w_{Ti}}{M_i} \frac{1}{\sum_j \frac{w_{Tj}}{M_j}} \quad (17)$$

131 The total amounts of iron and oxygen fixed by the iron can be expressed as:

$$132 \quad m_{Fe} = m_{FeO} + 2m_{Fe_2O_3}$$

$$133 \quad m_{O(Fe)} = m_{FeO} + 3m_{Fe_2O_3} \quad (18)$$

134 The oxygen fixed by the iron is thus:

$$135 \quad m_{O(Fe)} = m_{Fe} \frac{1+3F}{1+2F} \quad (19)$$

136 where the symbol $F = \frac{m_{Fe2O3}}{m_{FeO}}$ has been used. Using $w_{TFe} = \frac{w_{TFeO^*}}{M_{FeO}} M_{Fe}$ and the
 137 conversion (17) for w_{TFe} and $w_{TO(Fe)}$ yields the total amount of oxygen fixed by the
 138 iron:

$$139 \quad w_{TO(Fe)} = M_O \frac{w_{TFe}}{M_{Fe}} \frac{1+3F}{1+2F} \quad (20)$$

140 The mass balance can now be rigorously carried out by adding the 9 oxides, the
 141 volatiles species (w_{TO} , w_{TS} , w_{TH} , and w_{TC}), the total iron (w_{TFe}) and the oxygen fixed
 142 by the iron ($w_{TO(Fe)}$). The total molar fractions m_k can be updated using (17) and are
 143 used in (16) for the rest of the simulation. Because the system is closed, all the
 144 quantities involved in the mass balance, except w_{TO} and $w_{TO(Fe)}$, are considered
 145 constant. The reaction (15) imposes an exchange of oxygen between that locked in the
 146 iron-bearing species and that involved in the C-S-O-H redox reactions. The sum $w_{TO} +$
 147 $w_{TO(Fe)} = w_{TO(Total)}$, however, remains constant. Thus, using (20), the total amount of
 148 “free” oxygen w_{TO} can be related to fO_2 :

$$149 \quad w_{TO} = w_{TO(Total)} - \frac{m_{Fe} M_O}{\sum_j m_j M_j} \frac{1+3F}{1+2F} \quad (21)$$

150 The second step of the resolution is to solve the system each time pressure
 151 decreases. Mass conservation (1) and (11-14), chemical equilibrium (6-10), and
 152 solubility laws (5) are used jointly to solve for the eleven unknowns (molar fractions
 153 m_i , the total gas weight fraction w_{gT} , and the oxygen fixed by iron $w_{TO(Fe)}$).

154 The numerical resolution of (21) needs to be coupled with that of the C-S-O-H
 155 system. For each pressure step, solving for the redox equilibrium of the volatile
 156 species yields an fO_2 . After algebraically reducing the redox system to three
 157 conservation equations on w_{TO} , w_{TS} , and w_{TH} , respectively, we use a globally
 158 convergent Newton algorithm with analytically-determined Jacobian matrix such that

159 these three quantities are conserved to a precision typically $<10^{-6}$. This fugacity is
160 used in (16) and (21) to obtain a new amount of “free” oxygen. The redox equilibrium
161 of the volatile species is solved again with the updated w_{TO} , and the process is
162 conducted iteratively until desired precision (typically $<10^{-6}$ on w_{TO}) is reached. In
163 most cases, an under-relaxation factor of 0.2 is applied to the updated w_{TO} to ensure
164 convergence in 10 to 20 iterations, but some fine-tuning is needed for cases with
165 strong redox gradients. Precision lower than 10^{-4} on w_{TO} tend to cause numerical
166 oscillations on f_{O_2} , highlighting the sensitivity of the redox state to small variations
167 of the mass balance. Runs without Fe generally take less than an hour on a standard
168 PC computer, whereas Fe-bearing runs can take up to a few hours.

169 **Model assumptions and calibration against experimental data**

170 The approach we followed in building the present model arises from three
171 concerns: (1) relax the need to assume a redox buffer during decompression, (2)
172 tailoring the complexity of the thermodynamic model to the amount and precision of
173 experimental data available to calibrate it and (3) simplify the mathematics so as to
174 yield a computationally efficient code.

175 The first point brought us to carry out calculations at each pressure step by mass
176 conservation so that the redox state of the magma stems from chemical equilibrium in
177 the gas phase, solubility laws, and mass conservation. The existence of a chemical
178 liquid in which volatile species are dissolved is taken in account by the double
179 assumption of thermodynamic equilibrium between gas and liquid (i.e., fugacities of
180 species in the gas phase equal those in the liquid phase) and that species solubilities
181 are not interdependent. As mentioned earlier, the drawback is the inability to solve for
182 the crystallization of redox-controlling mineral phases such as magnetite or pyrrhotite.

183 The second point is illustrated by Fig. 1, which shows the predicted vs. measured
184 amounts of volatiles in the melt using our solubility laws. The parameter ranges
185 covered by the experimental data we used for model calibration are indicated in Table
186 2. Although simple, the model displays the ability to satisfactorily reproduce the
187 behavior of H₂O, H₂S, and CO₂. We considered the solubility of SO₂ temperature
188 independent because experimental data lack the trend necessary to derive such
189 dependence (see Clemente et al., 2004), as apparent in the greater scatter of the SO₂
190 data (Fig. 1). The choice of coupling empirical relationships on iron redox state (16)
191 and experimentally-calibrated solubility laws (3a) partially accounts for cross-effects
192 of species that were not considered in our model. For instance, interactions between
193 gaseous and liquid species of the H₂O-S system (e.g., Moretti and Ottonello, 2005) are
194 empirically represented through the calibration of our sulfur solubility laws with data
195 obtained on hydrous rhyolite (Table 2).

196 The assumptions of Henrian-like behavior of the volatile species and their ideal
197 mixing in their gaseous state imply that we neglect any cross-effects of the species in
198 determining their saturation content and their fugacities. As a result, our model has
199 been calibrated on a dataset centered around 2000 bars (Table 2), and is not expected
200 to give good results at higher pressure (>3000 bars), unlike more sophisticated
201 thermodynamic models (e.g., Papale, 1999; Moretti and Papale, 2004).

202 The last point led us, for instance, to choose Equ. (3a) over (3), so as to ease the
203 future integration of such a code into more realistic degassing and magma ascent
204 models (e.g., Dufek and Bergantz, 2005). The small impact of such a simplification is
205 illustrated by a typical decompression run, where differences between Equ. (3) and
206 (3a) are less than 0.2, 0.02, 0.004, 3, 3, 0.06, 0.03, 0.04, and 0.04 percent on $m_{\text{H}_2\text{O}}$,
207 m_{H_2} , m_{O_2} , m_{SO_2} , $m_{\text{H}_2\text{S}}$, m_{S_2} , m_{CO_2} , m_{CO} , and m_{CH_4} , respectively. These maximum errors

208 occur at high pressure (i.e. 1000 bars for a run starting at 2000 bars) for all species but
209 O₂, for which the maximum error occurs at the lowest pressure.

210 **Effects of decompression on the chemistry of arc magmas**

211 Decompression causes profound changes in the volatile distribution between melt
212 and gas. As a result, the chemical evolution of gas phase is complex, with the various
213 species changing their relative proportions by orders of magnitudes (Fig. 2). In this
214 work we highlight the general degassing patterns arising from decompressing arc
215 magmas instead of focusing on particular cases. The fundamental observation
216 sustaining such an approach is the recognition that Nature favors certain combinations
217 of intensive parameters at depth (e.g., restricted range of oxygen fugacities) and that
218 such combinations are not necessarily equally represented by the various experimental
219 studies (Table 2). We thus use our calibrated model to explore the range of natural
220 parameters so as to gather a general, first-order understanding of the geochemical
221 trends arising from magma decompression, ascent, and eruption in subduction arc
222 setting. We performed a parametric study that covers the natural range of conditions
223 at depth for arc volcanoes reported by Scaillet & Pichavant (2003, Table 2). Note that
224 we excluded Pine Grove ($P=4050$ bars, $T=675$ °C) from the list reported by Scaillet &
225 Pichavant (2003) so as to limit our scope to $P\leq 3000$ bars and $T\geq 720$ °C and avoid
226 extrapolating the model beyond the domain for which it was calibrated (see Model
227 assumptions and calibration against experimental data). Lower-than-calibrated
228 temperatures are used in some runs, as the linear trends we parameterized make such
229 extrapolation reasonable (Table 1).

230 The chemistry of the rhyolitic melt is based on that of the Panum Crater Dome (in
231 wt%: SiO₂=77.44, Al₂O₃=12.88, TiO₂=0.07, CaO=0.6, Na₂O=4.14, K₂O=4.76,
232 MgO=0.03, MnO=0.05, P₂O₅=0.03, Mangan & Sisson, 2000). We present the results

233 by first fixing total initial pressure to 2000 bars, the temperature to 825 °C, and FeO*
234 to 1 wt%. Two sets of runs were carried out under these common initial conditions.
235 The first set has an initial water fugacity of 1000 bars, which allows 4.43 wt% of
236 water to dissolve in the melt. The second set has an initial $f_{\text{H}_2\text{O}}$ of 1450 bars, or 5.41
237 wt% of water in the melt. In each set, we varied the initial H_2 and CO_2 fugacities so as
238 to cover the natural range of redox state, from NNO-0.5 to NNO+1.7, and C/S ratio
239 from 0.3 to 300 (Scaillet & Pichavant, 2003). Table 3 summarizes these 32 initial
240 conditions. Each of the simulations was run with little (0.1 wt%) and a large amount
241 (5 wt%) of initial gas, yielding 64 runs. Note that changing the initial gas content
242 affects the total amounts of elemental C, S, O, and H, as well as total amount of each
243 species, but does not influence other variables listed in Table 3. We then chose
244 representative runs from Table 3 and varied the initial pressure between 1000 and
245 3000 bars, the temperature between 720 and 930 °C, and the FeO* between 0 and 3
246 wt%, once again covering the range of values commonly found in arc volcanism
247 (Table 2). Water contents can be used to divide runs into two groups. Within each
248 group, when carbon is added at the expense of sulfur, the C/S ratio increases and
249 systems become depleted in sulfur. Thus, systems will be referred to indifferently by
250 their initial C/S ratios in the gas and by the relative amounts of S dissolved in the melt
251 (e.g., run 1 in Table 3 belongs to the H_2O -poor group and represents a S-rich system
252 with a low C/S ratio). As decompression progresses, important chemical changes take
253 place. We use three indicators to track the magnitude of those changes: the redox state
254 of the magma as measured by f_{O_2} , the $\text{H}_2\text{S}/\text{SO}_2$ and C/S ratios of the gas phase. At a
255 fixed pressure, the redox state of the magma is insensitive to the amount of carbon
256 present in the system. Thus, there is a direct relationship between the redox state as
257 measured by ΔNNO and $\text{H}_2\text{S}/\text{SO}_2$ when initial conditions are being set. Although this

258 ceases to be true when magma decompresses as a closed system, it is convenient to
259 consider these two indicators together.

260 Decompressions starting with little gas in the reservoir show one of the most
261 complex patterns of chemical variations. The redox evolution with decreasing
262 pressure of these gas-poor runs can be quite elaborate with the trend at high-pressure
263 often opposite to that at lower pressure, which causes characteristic S-shaped curves
264 that remind of those noted by Moretti and Papale (2004, Fig. 3A). We first use the
265 water-poor group (runs 1-16, Table 3) to further describe these trends. S-rich systems
266 (low C/S ratios) generally tend to converge towards the NNO buffer, changing their
267 initial redox state by as much as 1 log unit in doing so (thick lines, Fig. 3A). In other
268 words, initially oxidized systems (above the NNO buffer) tend to reduce, whereas
269 systems initially below NNO have weak redox variations. In S-poor systems, the
270 redox trend reverses such that it diverges from the NNO buffer; initially oxidized
271 systems become more oxidized at shallow pressure, whereas initially reduced systems
272 reduce further (stippled lines, Fig. 3A). The $\text{H}_2\text{S}/\text{SO}_2$ ratio shows a somewhat similar
273 pattern. S-rich systems display a quasi-monotonic decrease of their $\text{H}_2\text{S}/\text{SO}_2$ ratio, but
274 the amount of decrease is again controlled by the initial redox state (thick lines, Fig.
275 3B). $\text{H}_2\text{S}/\text{SO}_2$ typically drops less than an order of magnitude for oxidized systems
276 and two orders of magnitude for reduced systems. S-poor systems also decrease their
277 $\text{H}_2\text{S}/\text{SO}_2$, but the redox state acts in the opposite way (stippled lines, Fig. 3B).
278 Oxidized, S-poor systems see their $\text{H}_2\text{S}/\text{SO}_2$ drop by more than a factor 1000 at low
279 pressure, whereas reduced systems decrease theirs by only a factor 10.

280 Decompressions starting with high water content in the melt display behaviors
281 similar to water-poor decompressions (gray areas, Fig. 3). The most notable
282 difference between the two groups of runs is that variations are less pronounced in the

283 water-rich group. As a result, initially reduced systems tend to remain close to the
284 NNO buffer regardless of S content.

285 At high gas fraction in the reservoir, trends simplify remarkably; the magma
286 reduces itself monotonically of about 2 log unit, except for S-poor, oxidized magmas,
287 for which the reduction dampens at low pressure (Fig. 4A). The $\text{H}_2\text{S}/\text{SO}_2$ ratio
288 remains relatively constant, except once again in the case of S-poor, oxidized
289 magmas, for which the ratio decreases up to 2 orders of magnitude (Fig. 4B). We note
290 that the reducing trends are most pronounced for water-poor, reduced systems, which
291 translates into a slight increase in their $\text{H}_2\text{S}/\text{SO}_2$ ratio.

292 The C/S ratio of the gas phase shows a pattern quite distinct from the two previous
293 variables. In gas-poor systems, changes in C/S occur only at high pressure, between
294 2000 and 1000 bar, and C/S remains constant until atmospheric pressure is reached
295 (Fig. 5). S-rich systems have C/S variations of less than 65% (~ 0.2 log units), and S-
296 poor systems see their C/S ratio decrease systematically from 300 down to at least 100
297 and at most 20, depending on the initial redox state and water content. There is a
298 critical redox state above which C/S decreases and below which it increases. It is
299 mainly controlled by the initial C/S ratio, and weakly by the initial H_2O content. S-
300 rich systems display a critical state around NNO+0.5 for H_2O -poor systems and
301 NNO+1 for H_2O -rich systems, whereas it is always above NNO+1.7 for S-poor
302 systems.

303 At high gas fraction in the reservoir, buffering effects of the gas phase have the
304 greatest effects on the C/S ratio, which remains constant throughout the
305 decompression regardless of initial water content. This is because C/S varies only at
306 high pressure, where the initial increase of gas is felt the most: a decompression
307 starting with 0.1 wt% gas at 2000 bars has 2.2 wt% gas when it reaches 400 bars,

308 whereas a decompression starting with 5 wt% gas reaches only 7.3 wt% gas at 400
309 bars. In other words, changing the initial gas content from 0.1 to 5 wt% corresponds
310 to a 50 times increase at 2000 bars, whereas it translates into an increase of only 3
311 times at the lower pressure of 400 bars.

312 We assessed the role of iron dissolved in the melt by varying its amount from 0 to
313 3 wt%. Figure 6 shows runs for which iron content has the largest impact on
314 degassing chemistry. As expected, iron acts as a buffer with respect to oxygen,
315 dampening somewhat the changes in redox during decompression. This buffering
316 effect is systematically less than 0.75 log unit.

317 Varying the initial pressure from 1000 to 3000 bars causes little changes in
318 degassing patterns. At higher starting pressure, the initial trend reversal that forms the
319 base of the S-shaped curves in the ΔNNO vs. P and $\text{H}_2\text{S}/\text{SO}_2$ vs. P plots (Fig. 3)
320 becomes more distinct. Changes in C/S ratio during decompression become also more
321 pronounced with higher initial pressure.

322 Varying the magma temperature from 720 to 930 °C was done such that the initial
323 pressure, ΔNNO , and C/S in gas were identical to those of run 10 (Table 3). As a
324 result, the initial $\text{H}_2\text{S}/\text{SO}_2$ in gas decreased with increasing temperature chiefly
325 because H_2S becomes more soluble at higher temperatures while SO_2 solubility
326 remains constant (Table 1). High temperatures smooth the S-shape described by the
327 redox state as a function of pressure (Fig. 7A). The low-pressure convergence towards
328 NNO is maximal at the mid-temperature range (i.e. 825 °C). Temperature exerts some
329 control over the critical redox state above which C/S decreases and below which it
330 increases (Fig. 7B). Here again, the critical state occurs at a higher value (more
331 oxidized) value when the temperature is at mid-range (825 °C). These non-monotonic

332 behaviors are mostly due to the fact that H₂S and CO₂ have solubility trends opposed
333 to that of H₂O (Table 1).

334 Finally, we computed graphite activity using the equilibrium constant of the
335 reaction C + O₂ = CO₂ given by Ohmoto and Kerrick (1977). In all runs this activity
336 remains largely below unity, thus ruling out the presence of graphite under arc magma
337 conditions.

338 **Effects of chemical changes on the development of porosity** 339 **during magma ascent**

340 If a melt density is fixed, say $\rho_l=2200$ kg/m³ for a typical rhyolitic melt, the gas
341 volume fraction of the ascending magma, α , can be calculated from our model outputs
342 at each pressure according to:

$$343 \quad \alpha = \left[1 + \frac{MP(1 - w_{gT})}{RT\rho_l w_{gT}} \right]^{-1} \quad (22)$$

344 where R is the universal gas constant (8.3144 J/mole °K), and M is the average molar
345 mass of the gas phase:

$$346 \quad M = \sum_{i=1}^n x_i M_i \quad (23)$$

347 Our initial conditions at depth are such that gas density varies by a factor ~2,
348 depending on how much sulfur and carbon species are present. At atmospheric
349 pressure, gas density is always close to that of water vapor because the molar
350 proportion of H₂O is always >95%. One can thus expect that the effect of chemistry
351 on the evolution of magma density during closed-system ascent from a deep reservoir
352 to the surface is negligible because the largest density changes occur when gas
353 volume fraction is the lowest.

354 At low initial f H₂O, water dominates the composition of the gas phase more
355 rapidly when there is little initial gas ($m_{H_2O} > 0.9$ when $P < 1150$ bars) than when there
356 is a large amount of gas ($m_{H_2O} < 0.9$ regardless of pressure). Thus, the effect of initial
357 chemistry is controlled at low initial gas content by the initial melt water content,
358 which is directly fixed by the initial value of f H₂O (Fig. 8). By contrast, varying the
359 initial chemical conditions mostly affects the development of porosity of magmas
360 starting their ascent with a large amount of initial gas in the reservoir. As expected, at
361 equal pressure, magmas with more heavy gaseous species such as SO₂ or CO₂ will be
362 less porous.

363 These considerations brought us to study closely a specific case in which initial
364 chemistry has major effects on the development of porosity. It necessitates initiating
365 the ascent from shallow depth with a low amount of gas and a water-poor gas phase.
366 To illustrate this phenomenon, we choose to first fix the initial conditions of the
367 reference run close to the equilibrium composition of run 11 at 400 bars (Table 3).
368 Water depletion can be achieved by high amounts of either S- or C-bearing species.
369 Here we use CO₂, but similar results can be obtained using SO₂ instead. The reference
370 run thus starts with f H₂O = 350 bars, f H₂ = 0.64 bar, and f CO₂ = 25.27 bars, and we
371 impose 0.1 wt% gas (i.e. about 2 vol% porosity). FeO* was set to zero so as to speed
372 calculations up. This corresponds to a gas phase composed of 93.9 mol% H₂O, 5.6
373 mol% CO₂, and 0.5 mol% of the remaining 7 species, which allows us to simply use
374 the H₂O/CO₂ ratio as a proxy for gas composition. We then compare this reference
375 run to three simulations with initial gas composition progressively richer in CO₂: 37,
376 53, and 72 mol%, respectively (Fig. 9A). Note that the H₂O/CO₂ ratio of these
377 simulations covers the natural range of deep basaltic fluids encountered below silicic
378 systems (Scaillet, unpub. data, 2007).

379 In these shallow decompressions, the porosity profile changes dramatically as a
380 function of the initial chemistry (Fig. 9B). The lower the H₂O/CO₂ ratio is, the more
381 porosity increases in a sharp manner. At low H₂O/CO₂, a pressure threshold forms
382 above which magma density changes little and below which magma rapidly foams.
383 The same threshold exists for viscosity and ascent speed, which both increase super-
384 exponentially when crossing it. The threshold occurs roughly when total pressure
385 reaches the initial *f* H₂O. Taking that correlation as a rule, a magma starting with 72
386 mol% CO₂ reaches ~15 vol% porosity at 100 bars, whereas the reference run already
387 reaches that porosity at ~270 bars. This is corroborated by the way both H₂O and CO₂
388 exsolve during ascent (Fig. 10). The water content of the melt remains stable until the
389 threshold pressure, while the exsolution rate of CO₂ has an inflexion point at that
390 pressure. The relation between total pressure and *f* H₂O is not exact because we
391 assume a mixture of real gases, which causes fugacities to diverge somewhat from
392 partial pressures.

393 Discussion

394 Volatile exsolution in ascending magmas follows complex patterns inherited from
395 the initial conditions under which decompression started. Our results show that both
396 solubility laws and chemical reactions occurring in the gas phase have a first-order
397 effect on volatile exsolution. We found that temperature, initial pressure, and melt
398 iron content alter the amplitude of the chemical changes during ascent, but do not
399 change the general degassing patterns.

400 These patterns are controlled by the amount of gas, the amount of water in the
401 melt (and thus *f* H₂O), and two other degrees of freedom. Because of the way the
402 various chemical parameters are correlated in our model at fixed pressure, one of
403 these degrees of freedom is either of redox state, *f* H₂, or H₂S/SO₂, whereas the other

404 degree is either of f CO₂ or C/S. It is known that the H-O-S system also display
405 changes in the redox state of the magma during ascent (Burgisser & Scaillet, 2007).
406 When C/S<1, the H-O-S-C system reacts in a similar way to that of the H-O-S
407 system. This is consistent with f CO₂ acting as an independent variable. Note that
408 another set of seven independent, initial variables could have been chosen to initialize
409 the model. Not singling out the total content of each species (e.g., H₂O and CO₂,
410 Table 3) has the advantage to enable the use of the total amount of initial gas as a free,
411 independent parameter, which is a pertinent choice when addressing the behavior of
412 natural systems.

413 The role of initial water content can be understood by looking at simpler chemical
414 systems. The end-member of the water-rich systems studied herein is the O-H system,
415 which bears only H₂O, H₂, and O₂. Burgisser & Scaillet (2007) showed that this
416 system oxidizes greatly upon decompression, and that, as sulfur is added into the
417 magma at the expense of water, the melt becomes depleted in water and the resulting
418 S-O-H system reduces upon decompression. These findings seem to be also true in the
419 C-S-O-H system, because at equal initial gas content, water-poor systems almost
420 always follow more reduced trends than water-rich ones (Figs 2A and 3A).

421 It is possible to reduce somewhat the complexity of degassing patterns by
422 considering the role of initial gas content. Gas-rich systems are essentially showing
423 what happens to an isolated gas pocket during isothermal decompression. Following
424 Symonds et al. (1994), one could thus expect that in gas-rich systems, the chemical
425 balance of the gas dictates a general reduction during decompression with an
426 associated drop in H₂S/SO₂ and does not affect the C/S ratio. This is always true for
427 the reducing trend and C/S. The H₂S/SO₂ evolution, however, is not entirely
428 dominated by the initial gas content, as it also depends on the initial redox state, C/S

429 and H₂O content (Fig. 3B). Gas-poor systems are chiefly dominated by solubility
430 laws. All four degrees of freedom exert considerable control under gas-poor
431 conditions. In particular, the presence of dissolved sulfur buffers the magnitude of
432 redox changes and drives systems towards NNO, whereas dissolved carbon draws
433 systems away from it. The schematic influence of these four degrees of freedom on
434 the redox patterns of decompressing rhyolites are summarized in Fig. 11.

435 Based on our model outputs, what traces of this complex degassing process can we
436 hope to measure in natural rocks? The limiting factor in that regard is the minimum
437 volatile content that can be measured in the natural glass. The most common
438 analytical technique, electron microprobe, can typically measure S contents larger
439 than 50 to 100 ppm. Lower detection limits of 1 to 10 ppm are achieved with more
440 recent techniques such as Secondary Ion Mass Spectroscopy (SIMS; Hauri et al.,
441 2002), or Fourier Transform InfraRed (FTIR; Stöpler and Holloway, 1988).
442 Inspection of typical evolution of total S and CO₂ dissolved in melt during
443 decompression shows that volatiles drop below microprobe detection limit soon after
444 leaving the reservoir (Fig. 12). Only the most sensitive techniques such as SIMS could
445 possibly detect degassing trends occurring in the conduit, between the reservoir and
446 100 bars. Volatiles remaining at shallow levels, within the dome, are often below 100
447 ppb.

448 Measurements of volcanic gases at active volcanoes use various techniques to
449 acquire different gas species, making inter-comparisons challenging (Aiuppa et al.,
450 2004, 2007). In particular, difficulties in converting between total sulfur and SO₂
451 measures strongly impede our ability to efficiently combine measuring techniques.
452 CO₂ fluxes, for example, are generally deduced by combining SO₂ flux measures
453 from the plume and independent, instant measures of sulfur and carbon species at the

454 vent (e.g., Fischer et al., 1996; Wardell et al., 2001; Goff et al., 2001). Too often,
455 however, punctual analyses give C/S ratio instead of CO₂/SO₂ ratio. This introduces
456 large uncertainties into the flux calculation because other sulfur species such as H₂S
457 affect total sulfur content, invalidating S as a reliable proxy for SO₂ (Aiuppa et al.,
458 2005). Thus, much can be learned on C/S to CO₂/SO₂ conversions by comparing
459 ratios from our model runs.

460 Our model outputs at atmospheric pressure do not represent gas composition
461 emitted at vent but the gas composition at equilibrium with a magma decompressed in
462 closed system. In other words, natural gases have been physically separated from the
463 magma they issued, but not in our degassing model. Keeping this distinction in mind,
464 we compared our calculated CO₂/SO₂ and C/S ratios at atmospheric pressure (Fig.
465 13). Differences between these two ratios are largest for gas-rich systems: CO₂/SO₂ is
466 one to three orders of magnitude higher than C/S. This is readily explained by the fact
467 that these runs have the largest amounts of H₂S in the gas phase (Fig. 4B). When little
468 H₂S is present, like in gas-poor, water-rich systems (Fig. 3B), the difference is less
469 than a factor two. This suggests that obtaining CO₂ fluxes from SO₂ flux
470 measurements at volcanoes where only the C/S ratio is available can largely
471 underestimate the CO₂ output if the reservoir contains a large amount of gas. Our runs
472 show that CO₂/SO₂ changes during decompression are not restricted to pressures
473 >1000 bars like in the case of C/S, but occur down to atmospheric pressure. The
474 content of SO₂ being strongly related to redox state, we observe the same partitioning
475 between gas content in the reservoir and initial melt water content than in the case of
476 redox evolution (Figs 3-4). Thus, CO₂/SO₂ is much more prone to be affected by
477 shallow degassing processes than C/S.

478 Volatile chemistry can greatly affect the way magma flows at shallow levels.
479 Under certain circumstances, we showed that exsolution can happen suddenly,
480 causing a brutal acceleration of the magma. It is important to understand how likely
481 such circumstances are because of the implications of such behavior on the explosive
482 potential of domes. First, a porosity lower than that at equilibrium is required. The
483 presence of low porosity at shallow level is not unreasonable in regions where bubble
484 collapse and permeability phenomenon have been shown to occur (e.g., Eichelberger
485 et al., 1986). Second, the magma must be water poor. It is possible to deplete magma
486 in H₂O by flushing the system with CO₂- and SO₂-rich gases. Syn-eruptive occurrence
487 of CO₂-rich volatiles issued from deep mafic recharges is likely to occur at many arc
488 volcanoes (Wallace, 2005). Such gas- and water-poor conditions are not restricted to
489 but can be believably achieved during a dome-forming eruption if the deep volatiles
490 percolate through the volcanic conduit and flush the slowly growing dome. Such
491 leaching has been proposed to occur at Popocatepetl lava dome, although in this case
492 the source of CO₂ remains unclear (Goff et al., 2001; Witter et al., 2005), and at
493 Soufrière Hills volcano, Montserrat (Edmonds et al., 2003), where a percolating flux
494 SO₂ as been assigned to a deep source. Our model does not simulate crystallization, so
495 the preferred scenario is a dome rapidly resuming its growth after a short repose
496 period, such as has been the case at Soufrière Hills throughout its on-going eruption
497 (Watts et al., 2002).

498 Our simulations indicate that further upward motion of the leached magma is
499 highly nonlinear. Model outputs show that the dome growth becomes highly unstable,
500 possibly leading to a violent exsolution event if the bubble-poor magma resuming
501 ascent flows past a critical pressure threshold. Another direct implication is that the
502 threshold, when present, may delimit which part of the magma column will be ejected

503 during a sudden decompression, such as caused by dome collapse or accompanying a
504 Vulcanian explosion.

505 **Conclusions**

506 We presented a coupled chemical-physical model of magma ascent based on nine
507 volatile species part of S-O-H-C-Fe-bearing rhyolitic melts. We conducted a
508 parametric study of degassing by varying the initial conditions at depth within the
509 range typical of arc magmas and characterizing the chemical and physical evolution
510 of rhyolitic melts during their ascent to the surface. This parametric study reduced
511 somewhat the complex and rich patterns of chemical evolution during ascent, as some
512 elements and variables have a restricted influence on the degassing process.

513 Initial values of four main parameters control the degassing patterns of volatile-
514 bearing rhyolites: ΔNNO , gas amount, melt water content and melt sulfur content.
515 Because of the way the various chemical parameters are correlated at fixed pressure
516 and temperature, the melt water content is directly related to $f\text{H}_2\text{O}$, the redox state is
517 related to $f\text{H}_2$ and gaseous $\text{H}_2\text{S}/\text{SO}_2$, and the relative sulfur content is related to $f\text{CO}_2$
518 and gaseous C/S.

519 Gas content exerts a strong control over the resulting degassing trends. A large
520 amount of gas imposes a reducing trend by minimizing the role of dissolved volatiles.
521 Melt H_2O , S, and CO_2 contents exert a weaker and more subtle control. At equal
522 initial gas content, water-poor systems almost always follow more reduced trends than
523 water-rich ones. On the other hand, S-rich systems tend to evolve towards the NNO
524 buffer, whereas S-poor systems tend to be drawn away from it. The initial redox state
525 exerts a variable control: the furthest away from the NNO buffer the rhyolite initially
526 is, the more the trend resulting from the other controls is heavily felt. Temperature,

527 initial pressure, and melt iron content alter the amplitude of the chemical fluctuations
528 during ascent, but do not change the general degassing patterns.

529 Volatile chemistry has little effect on the amount of degassing during closed-
530 system, equilibrium degassing from a deep reservoir. The evolution of porosity at
531 shallow levels, however, can be greatly affected by degassing chemistry. It requires
532 that the magma starts with a porosity lower than that at equilibrium and that it is
533 strongly depleted in water compared to the other species (e.g., CO₂ and SO₂). Further
534 upward motion of such shallow-seated magma is subject to sudden, massive
535 degassing when the magma flows past a critical pressure threshold. This scenario best
536 applies to domes resuming rapidly their growth after a short repose period.

537 **Acknowledgments**

538 This study was partly supported by the French Program ANR-EXPLANT
539 (contract No ANR-05-CATT-003 to C. Martel). We thank the in-depth reviews of R.
540 Moretti and an anonymous reviewer, which improved the manuscript.

References

- Aiuppa, A., Burton, M., Murè, F., and Inguaggiato, S. (2004) Intercomparison of volcanic gas monitoring methodologies performed on Vulcano Island, Italy, *Geophysical Research Letters*, v.31,L02610.
- Aiuppa, A., Inguaggiato, S., McGonigle, A.J.S., O'Dwyer, M., Oppenheimer, C., Padgett, M.J., Rouwet, D., and Valenza, M. (2005) H₂S fluxes from Mt. Etna, Stromboli, and Vulcano (Italy) and implications for the sulfur budget at volcanoes, *Geochimica et Cosmochimica Acta*, v.69, p.1861-1871.
- Aiuppa A., Moretti R., Federico C., Giudice G., Guerrieri S., Liuzzo M., Shinohara. H. (2007) Forecasting Etna eruptions by real-time observation of volcanic gas composition, *Geology*, v.35, p.1115-1118
- Blank, J.G., Stople, E.M., and Carroll, M.R. (1993) Solubilities of carbon dioxide and water in rhyolitic melt at 850 °C and 750 bars, *Earth and Planetary Science Letters*, v.119, p.27-36.
- Burgisser, A., and Scaillet, B. (2007) Redox evolution of a degassing magma rising to the surface, *Nature*, v.445, p.194-197.
- Clemente, B., Scaillet, B. & Pichavant, M. (2004) The solubility of sulphur in hydrous rhyolitic melts. *J. Petrol.* 45, 2171-2196.
- Delmelle, P., and Stix, J. (2000) Volcanic gases, in: Sigurdsson, H. (ed) *Encyclopedia of volcanoes*, Academic Press, p.803-815.
- Dufek, J., and Bergantz, G.W. (2005) Transient two-dimensional dynamics in the upper conduit of a rhyolitic eruption: A comparison of closure models for the granular stress, *Journal of Volcanology and Geothermal Research*, v.143, p.113-132.
- Edmonds, M., Oppenheimer, C., Pyle, D.M., Herd, R.A., and Thompson, G. (2003) SO₂ emissions from Soufrière Hills Volcano and their relationship to conduit permeability, hydrothermal interaction and degassing regime, *Journal of Volcanology and Geothermal Research*, v.124, p.23-43.
- Eichelberger, J.C., Carrigan, C.R., Westrich, H.R., and Price, R.H. (1986) Non-explosive silicic volcanism, *Nature*, v.323, p.598-602.
- Fischer, T.P., Arehart, G.B., Sturchio, N.C., and Williams, S.N. (1996) The relationship between fumarole gas composition and eruptive activity at Galeras Volcano, Colombia, *Geology*, v.24, p.531-534.
- Gaillard, F., Pichavant, M., and Scaillet, B. (2003a) Experimental determination of activities of FeO and Fe₂O₃ components in hydrous silicic melts under oxidizing conditions, *Geochim Cosmochim. Acta*, v. 67, p.2427-2441.
- Gaillard, F., Schmidt, B. Mackwell, S. and McCammon, C. (2003b) Rate of hydrogen-iron redox exchange in silicate melts and glasses. *Geochim Cosmochim. Acta*, v. 67, 2427-2441.
- Gardner, J.E., Hilton, M., and Carroll, M.R. (1999) Experimental constraints on degassing of magma: Isothermal bubble growth during continuous decompression from high pressure, *Earth and Planetary Science Letters*, v.168, p.201-218.
- Ghiorso, M.S., and Sack, R.O. (1995) Chemical mass transfer in magmatic processes. iv. a revised and internally consistent thermodynamic model for the interpolation and extrapolation of liquid-solid equilibria in magmatic systems at elevated temperatures and pressures, *Contributions to Mineralogy and Petrology*, 119, 197-212
- Goff, F., Love, S.P., Warren, R.G., Counce, D., Obenholzner, J., Siebe, C., and Schmidt, S.C. (2001) Passive infrared remote sensing evidence for large, intermittent CO₂ emissions at Popocatepetl volcano, Mexico, *Chemical Geology*, v.177, p.133-156.
- Hauri, E., Wang, J., Dixon, J.E., King, P.L., Mandeville, C., and Newman, S. (2002) SIMS analysis of volatiles in silicate glasses 1. Calibration, matrix effects and comparisons with FTIR, *Chemical Geology*, v.183, p.99-114.

- Holland T., & Powell, R. (1991) A Compensated-Redlich-Kwong (CORK) equation for volumes and fugacities of CO₂ and H₂O in the range 1 bar to 50 kbar and 100-1600°C, *Contributions to Mineralogy and Petrology* v.109, p.265-273.
- Holtz, F., Behrens, H., Dingwell, D.B. & Johannes, W. H₂O solubility in haplogranitic melts: compositional, pressure and temperature dependence. *Am. Mineral.* 80, 94-108 (1995).
- Kress, V.C., and Carmichael, I.S.E. (1991) The compressibility of silicate liquids containing Fe₂O₃ and the effect of composition, temperature, oxygen fugacity and pressure on their redox states, *Contributions to Mineralogy and Petrology*, v.108, p. 82-92.
- Mangan, M., and Sisson, T. (2000) Delayed, disequilibrium degassing in rhyolite magma: decompression experiments and implications for explosive volcanism, *Earth and Planetary Science Letters*, v.183, p.441-455.
- Moretti, R. (2005) Polymerisation, basicity, oxidation state and their role in ionic modelling of silicate melts, *Annals of Geophysics*, v.48, p.583-608.
- Moretti, R., and Papale, P. (2004) On the oxidation state and volatile behavior in multicomponent gas-melt equilibria, *Chemical Geology*, v.213, p.265-280.
- Moretti, R., and Ottonello, G. (2005) Solubility and speciation of sulfur in silicate melts: The Conjugated Toop-Samis-Flood-Grjotheim (CTSFG) model, *Geochimica et Cosmochimica Acta*, v.69, p.801-823.
- Moretti, R., Papale, P., and Ottonello, G. (2003) A model for the saturation of C-O-H-S fluids in silicate melts, in: Oppenheimer, C, Pyle, D.M., Barclay, J. (eds) *Volcanic degassing*, Geological Society Special Publication 213, London, p.81-101.
- Newman, S., and Lowenstern, J.B. (2002) VolatileCalc: a silicate melt-H₂O-CO₂ solution model written in Visual Basic for Excel, *Computers & Geosciences*, v.28, p.597-604.
- Ohmoto, H., and Kerrick, D.M. (1977) Devolatilisation equilibria in graphitic systems, *American Journal of Science*, v.277, p. 1013-1044.
- Ottonello, G., Moretti, R., Marini, L., and Vetuschi Zuccolini, M. (2001) Oxidation state of iron in silicate glasses and melts: a thermochemical model, *Chemical Geology*, v.174, p.157-159.
- Papale, P. (1999) Modeling of the solubility of a two-component H₂O+CO₂ fluid in silicate liquids, *American Mineralogist*, v.84, p.477-492.
- Papale, P. (2005) Determination of total H₂O and CO₂ budgets in evolving magmas from melt inclusion data, *Journal of Geophysical Research*, v.110, B03208.
- Papale, P., and Polacci, M. (1999) Role of carbon dioxide in the dynamics of magma ascent in explosive eruptions, *Bulletin of Volcanology*, v.60, p.583-594.
- Papale, P., Moretti, R., and Barbato, D. (2006) The compositional dependence of the saturation surface of H₂O+CO₂ fluids in silicate melts, *Chemical Geology*, v.229, p.78-95.
- Scaillet, B., and Pichavant, M. (2003) Experimental constraints on volatile abundances in arc magmas and their implications for degassing processes, in: Oppenheimer, C, Pyle, D.M., Barclay, J. (eds) *Volcanic degassing*, Geological Society Special Publication 213, London, p.23-52.
- Shaw, H.R., and Wones, D.R. (1964) Fugacity coefficients for hydrogen gas between 0° and 1000° C, for pressures to 3000 ATM, *American Journal of Science*, v. 262, p. 918-929.
- Shi, P.F. & Saxena, F.K. (1992) Thermodynamic modeling of the C-H-O-S fluid system. *Amer. Mineral.* 77, 1038-1049.
- Stöpler, E., and Holloway, J.R. (1988) Experimental determination of the solubility of carbon dioxide in molten basalt at low pressure, *Earth and Planetary Science Letters*, v.87, p. 397-408.
- Symonds, R.B., and Reed, M.H. (1993) Calculations of multicomponent chemical equilibria in gas-solid-liquid systems: calculation methods, thermochemical data, and applications to studies of high-temperature volcanic gases with example of Mount St. Helens, *American Journal of Science*, v.293, p.758-864.
- Symonds, R.B., Rose, W.I., Bluth, G.J.S., and Gerlach, T.M. (1994) Volcanic-gas studies: methods, results, and applications, in: Carroll, M.R., and Holloway, J.R. (eds) *Volatiles in magmas*, *Reviews in Mineralogy*, v. 30, p.1-66.

- Wallace, P.J. (2005) Volatiles in subduction zone magmas: concentrations and fluxes based on melt inclusions and volcanic gas data, *Journal of Volcanology and Geothermal Research*, v.140, p.217-240.
- Watts, R.B., Herd, R.A., Sparks, R.S.J., and Young, S.R. (2002) Growth patterns and emplacement of the andesitic lava dome at Soufrière Hills volcano, Montserrat, in: Druitt, T.H. and Kokelaar, B.P. (eds) *The eruption of Soufriere Hills Volcano, Montserrat, from 1995 to 1999*, Geological Society, London, *Memoirs*, v. 21, p.115-152.
- Wardell, L.J., Kyle, P.R., Dunbar, N., and Christenson, B. (2001) White Island volcano, New Zealand: carbon dioxide and sulfur dioxide emission rates and melt inclusion studies, *Chemical Geology*, v.177, p.187-200.
- Witter, J.B., Kress, V.C., and Newhall, C.G. (2005) Volcan Popocatepetl, Mexico. Petrology, magma mixing, and immediate sources of volatiles for the 1994-present eruption, *Journal of Petrology*, v.46, p.2337-2366.
- Young, S.R., Voight, B., and Duffell, H.J. (2003) Magma extrusion dynamics revealed by high-frequency gas monitoring at Soufrière Hills volcano, Montserrat, in: Oppenheimer, C, Pyle, D.M., Barclay, J. (eds) *Volcanic degassing*, Geological Society Special Publication 213, London, p.219-230.

Table 1: Solubility constants used in the degassing model. Temperatures are in °C.

The a_i and b_i parameters were determined by fitting experimental solubility data of corresponding species to an empirical equation of the form $w_i = a_i f_i^{b_i}$. We have used data from Clemente et al. (2004) for sulfur bearing species in hydrous rhyolites, Holtz et al. (1992, 1995) for H₂O, Fogel and Rutherford (1990) and Blank et al. (1993) for CO₂, and Gaillard et al. (2003b) for H₂ (see Table 2 for experimental ranges).

species	a_i	b_i
H ₂ O	$-4.69 \cdot 10^{-6} T + 4.81445 \cdot 10^{-3}$	$7.2827 \cdot 10^{-4} T - 4.276384 \cdot 10^{-2}$
H ₂	$3.400 \cdot 10^{-7}$	1.2800
SO ₂	$1.632 \cdot 10^{-10}$	1.3789
H ₂ S	$9.1668 \cdot 10^{-9} T + 4.204306 \cdot 10^{-7}$	$5.347 \cdot 10^{-4} T + 8.67136 \cdot 10^{-2}$
CO ₂	$1.046 \cdot 10^{-9} T - 4.5124 \cdot 10^{-7}$	$-6.738 \cdot 10^{-4} T + 1.628$
CO	0	-
CH ₄	0	-
O ₂	0	-
S ₂	0	-

Table 2: Parameter ranges. The five first columns show ranges of experimental parameters used to calibrate the chemical model. The last column indicates the range of initial conditions derived from data on natural arc magmas that we used in the parametric study.

Parameter	H ₂ S ^a	SO ₂ ^a	H ₂ O ^b	CO ₂ ^c	H ₂ ^d	Natural range ^e
ΔNNO	-2.26 – 0	1 – 2.91	>0	~1	n.a.	-0.5 – 1.7
C/S in gas	n.a.	n.a.	n.a.	n.a.	n.a.	0.3 – 300
P (bar)	2000	2000	500 – 3000	500 – 2500	220 – 265	1000 – 3000
f _i (bars)	1 – 5000	10 ⁻³ – 8000	500 – 3000	45 – 5000	0.02 – 70	n.a.
T (°C)	800 – 1000	800 – 1000	800 – 900	850 – 1050	700 – 1000	725 – 925
FeO* (wt%)	0.05 – 2.11	0.07 – 3.26	0-0.61	0.38 – 1	0.08 – 1.6	0 – 3
H ₂ O _{melt} (wt%)	1.92 – 6.78	1.78 – 6.74	2 – 6	0.51-3.34	n.a.	4.43 – 5.41

n.a.: not applicable.

^aClemente et al. (2004); ^bHoltz et al. (1992, 1995); ^cFogel and Rutherford (1990) and Blank et al. (1993); ^dGaillard et al. (2003b); ^eScaillet and Pichavant (2003).

Table 3. Initial conditions for the parametric study. All runs start with a rhyolite at 2000 bars and 825 °C with 1 wt% FeO*. Only $f_{\text{H}_2\text{O}}$, f_{H_2} , and f_{CO_2} are set, the other variables in the table are calculated by the chemical model. Each run was carried out with 0.1 and 5 wt% initial gas, and ratios are given in molar fraction. Dissolved water contents are in wt% and other dissolved species are in ppm.

Run	$f_{\text{H}_2\text{O}}$	f_{H_2}	f_{CO_2}	ΔNNO	C/S	H ₂ S/SO ₂	S	CO ₂	H ₂ O	C/S	total H ₂ O		total CO ₂		total S	
	bar	gas	melt								melt	melt	0.1 wt%	5 wt%	0.1 wt%	5 wt%
1	1000	10	2.9	-0.54	0.31	965	238	1.35	4.46	0.00154	4.51	6.97	3	79	661	20690
2	1000	10	9.2	-0.54	3.0	965	134	4.55	4.46	0.00929	4.52	7.42	10	295	296	7966
3	1000	10	11.84	-0.54	30	965	46.4	5.94	4.46	0.0349	4.53	7.67	14	410	69	1130
4	1000	10	12.187	-0.54	304	965	14.5	6.13	4.46	0.116	4.53	7.70	14	426	17	128
5	1000	5	41	0.06	0.31	121	237	22.0	4.46	0.0253	4.51	6.92	43	1094	657	20525
6	1000	5	131	0.06	3.1	121	133	75.1	4.46	0.154	4.52	7.28	155	4007	286	7543
7	1000	5	168	0.06	31	121	45.9	97.6	4.46	0.580	4.52	7.46	207	5461	66	1044
8	1000	5	172.81	0.06	303	121	14.5	101	4.46	1.90	4.52	7.48	214	5664	16	121
9	1000	1.7	304	1	0.3	4.7	216	183	4.46	0.23	4.51	6.57	326	7023	591	18362
10	1000	1.7	956	1	3	4.7	121	612	4.46	1.37	4.51	6.56	1073	22026	239	5780
11	1000	1.7	1228	1	31	4.7	42.2	797	4.46	5.15	4.51	6.55	1391	28153	57	753
12	1000	1.7	1263.8	1	301	4.7	13.2	821	4.46	16.9	4.51	6.55	1432	28950	14	87
13	1000	0.75	328	1.71	0.3	0.41	161	198	4.46	0.334	4.50	6.26	331	6496	472	15450
14	1000	0.75	1041	1.71	3	0.41	78.7	669	4.46	2.32	4.50	6.41	1139	22264	185	5322
15	1000	0.75	1340	1.71	31	0.41	25	874	4.46	9.5	4.50	6.47	1501	29611	39	709
16	1000	0.75	1379.1	1.71	303	0.41	7.72	901	4.46	31.8	4.50	6.48	1549	30607	9	79
17	1450	14.6	0.33	-0.54	0.31	1429	116	0.136	5.49	0.00032	5.58	9.77	0.3	10	239	6046
18	1450	14.6	1.05	-0.54	3	1429	65	0.461	5.49	0.0019	5.58	9.97	1	35	108	2095
19	1450	14.6	1.355	-0.54	30	1429	22.7	0.603	5.49	0.0072	5.58	10.06	1	46	28	288
20	1450	14.6	1.3953	-0.54	300	1429	7.08	0.622	5.49	0.024	5.58	10.07	2	48	7	34
21	1450	7.3	5.02	0.06	0.3	179	118	2.4	5.49	0.00556	5.58	9.74	5	159	244	6214
22	1450	7.3	16.3	0.06	3	179	65.9	8.32	5.49	0.0345	5.58	9.93	19	540	109	2122
23	1450	7.3	20.99	0.06	30	179	23	10.9	5.49	0.129	5.58	10.01	25	708	28	293
24	1450	7.3	21.614	0.06	302	179	7.14	11.2	5.49	0.429	5.58	10.02	25	731	7	35
25	1450	2.46	69	1	0.3	6.8	111	38.2	5.49	0.0936	5.57	9.57	80	2104	235	6096
26	1450	2.46	223	1	3	6.8	62.3	132	5.49	0.576	5.57	9.55	269	6789	102	1988
27	1450	2.46	287.4	1	30	6.8	21.7	172	5.49	2.16	5.57	9.55	349	8739	27	269
28	1450	2.46	295.96	1	303	6.8	6.72	177	5.49	7.2	5.57	9.54	360	8998	7	32
29	1450	1.09	83	1.71	0.3	0.59	76.6	46.4	5.49	0.165	5.57	9.33	94	2389	191	5725
30	1450	1.09	266	1.71	3	0.59	41.3	159	5.49	1.05	5.57	9.42	317	7834	79	1908
31	1450	1.09	342.7	1.71	30	0.59	14.1	207	5.49	4	5.57	9.45	414	10188	19	256
32	1450	1.09	352.88	1.71	301	0.59	4.37	214	5.49	13.3	5.57	9.46	427	10504	5	29

Figure caption

Figure 1: Measured vs. calculated volatile melt concentration. Data sources and solubility laws are listed in Table 1. Concentrations have been normalized to 1300 ppm, 6 wt%, 1200 ppm, and 800 ppm for CO₂, H₂O, H₂S, and SO₂, respectively. Hydrogen was not included, as melt concentrations reported by Gaillard et al. (2003b) do not correspond to actual measurements.

Figure 2: Gas composition of a typical decompression run with a rhyolitic melt starting at Δ NNO +1 with 0.1 wt% gas in the reservoir, 121 ppm S and 612 ppm CO₂ in the melt. Note that O₂ is not shown owing to its minute content. With a total pressure of 2000 bar in the reservoir, these volatile contents correspond to initial fugacities of 1000, 1.7, and 956 bars for H₂O, H₂, and CO₂, respectively (run 10, Table 3). These conditions are close to those at Mt. St. Helens during the 1980 eruptions.

Figure 3: Evolution of redox state (A) and the H₂S/SO₂ ratio of the gas phase (B) of a decompressing rhyolite starting from a gas-poor (0.1 wt%) reservoir. Runs start with either water-poor (black lines) or water-rich (gray areas) rhyolites.

Figure 4: Evolution of redox state (A) and the H₂S/SO₂ ratio of the gas phase (B) of a decompressing rhyolite starting from a gas-rich (5 wt%) reservoir. Runs start with either water-poor (black lines) or water-rich (gray areas) rhyolites.

Figure 5: Evolution of the C/S ratio of the gas phase decompressing in equilibrium with a rhyolitic melt. Runs start from a gas-poor reservoir with either water-poor (black lines) or water-rich (gray areas) rhyolites.

Figure 6: Variations in redox pattern of a decompressing rhyolitic melt as a function of FeO* content. Runs start from a gas-poor reservoir with a C/S ratio of 0.3 (FeO* = 1 wt% is run 13, Table 3).

Figure 7: Variations in redox pattern (A) and C/S ratio of the gas phase (B) of a decompressing rhyolitic melt as a function of temperature. The fugacities of H₂O, H₂ and CO₂ were adjusted so that H₂O_{melt}, ΔNNO, and C/S_{gas} match those of the reference run (run 10, Table 3).

Figure 8: Evolution of gas volume fraction of a decompressing rhyolitic melt as a function of total pressure.

Figure 9: Effects of initial gas composition on a decompression from shallow level. Evolution of gas composition (A) and gas volume fraction (B) with pressure. The reference run (thick line, f H₂O = 350 bars) starts with an equilibrium composition close to run 11 at 400 bars (Table 3). The three other runs have an initial gas composition progressively richer in CO₂. The gray vertical lines indicate the respective initial f H₂O of each run. These lines also correspond to a pressure threshold below which magma massively degasses.

Figure 10: Evolution of melt water content (A) and CO₂ exsolution rate (B) during a decompression from shallow level. The gray vertical lines indicate the respective initial f H₂O of each run, which are the same as in Figure 9.

Figure 11: Schematic influences of the four main controls (ΔNNO, gas, melt water content and melt sulfur content) of degassing patterns of volatile-bearing rhyolites. Relative initial values of these controls each influence the redox evolution during decompression in the direction shown by the arrows (circle = buffering effect). The control can be strong (heavy arrows for gas content), modest (light arrows for sulfur content), or variable (for ΔNNO, the furthest away from the NNO buffer the rhyolite is, the more the trend resulting from the other controls is heavily felt).

Figure 12: Evolution of S and CO₂ dissolved in a rhyolitic melt during degassing of gas-rich, water-poor systems. The fields cover S and CO₂ melt content for the whole range of initial redox conditions (from NNO-0.5 in stippled lines to NNO+1.7 in solid lines). The S field corresponds to C-poor, S-rich runs (1, 5, 9, and 13; Table 3) and the CO₂ field corresponds to C-rich, S-poor runs (4, 8, 12, and 16), thus maximizing the respective content of each component. Detection limits of common analytical methods and typical pressure ranges encountered in domes and volcanic conduits are also shown.

Figure 13: Ratios of C/S and CO₂/SO₂ in the gas phase at atmospheric pressure for all runs of the parametric study. Runs have been classified along the y-axis by quantity of gas at depth and initial melt water content. The initial oxidation state is shown as a gradient for C/S (lightest is most reduced at NNO-0.5) and as an arrow for CO₂/SO₂ (arrow points towards most reduced).

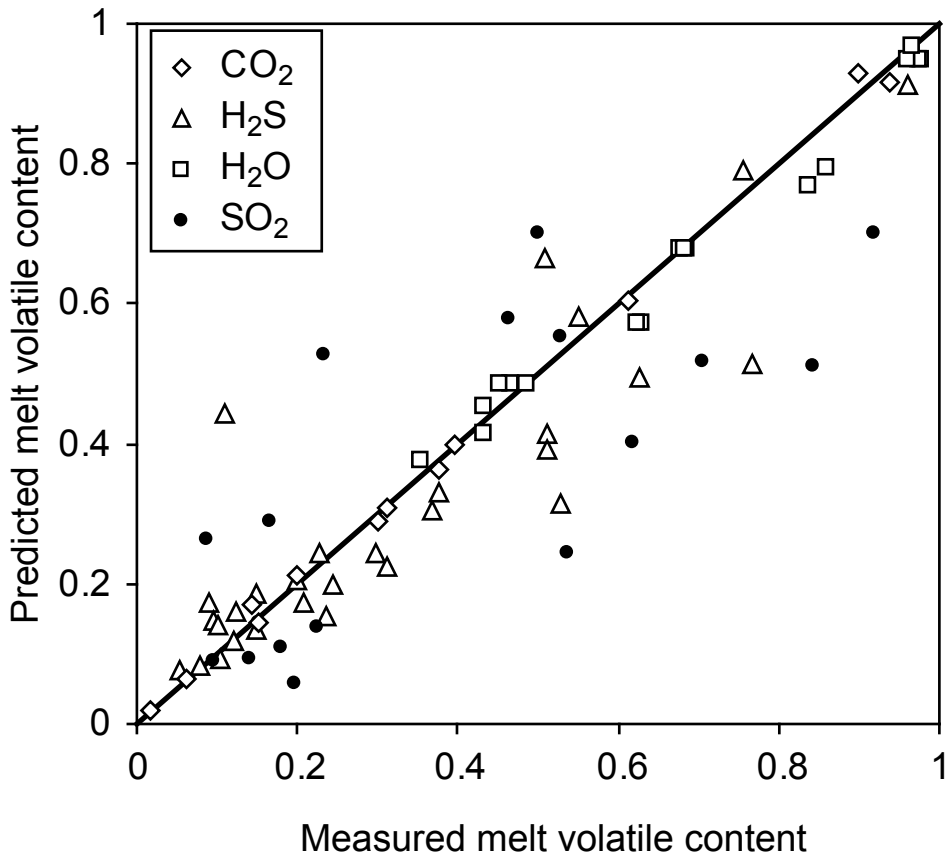


Figure 1

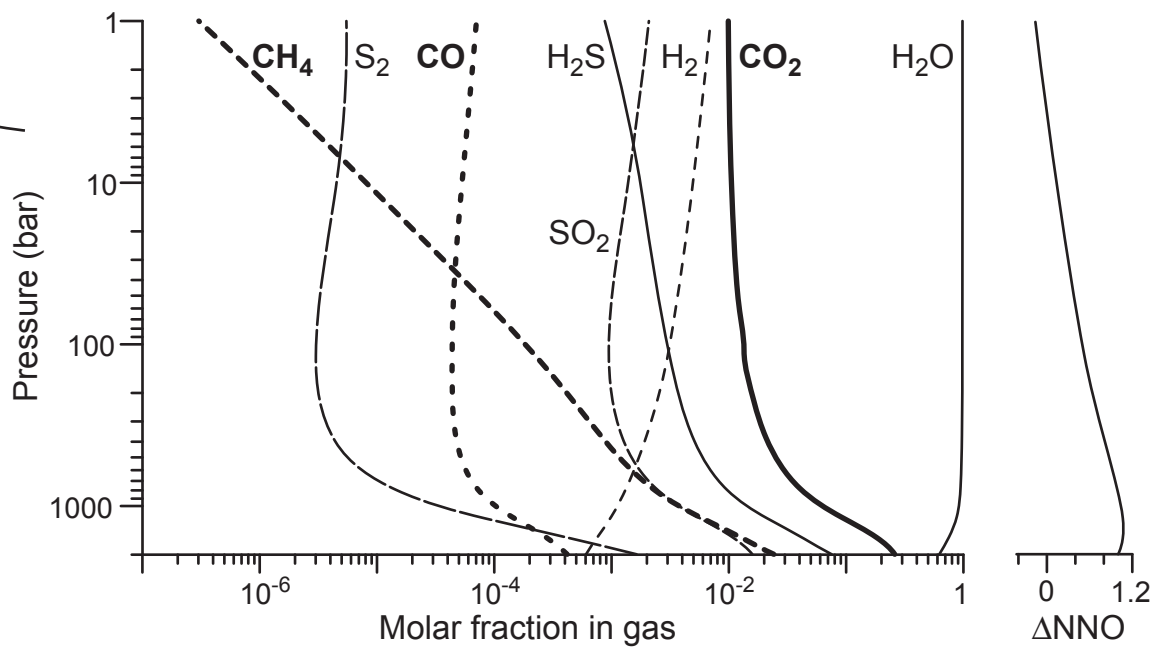
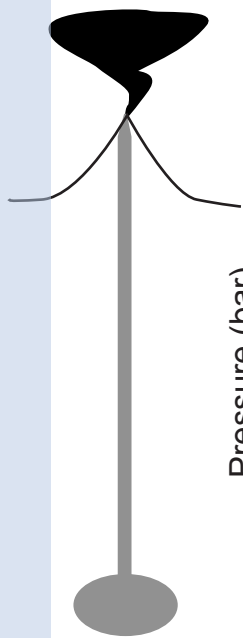


Figure 2

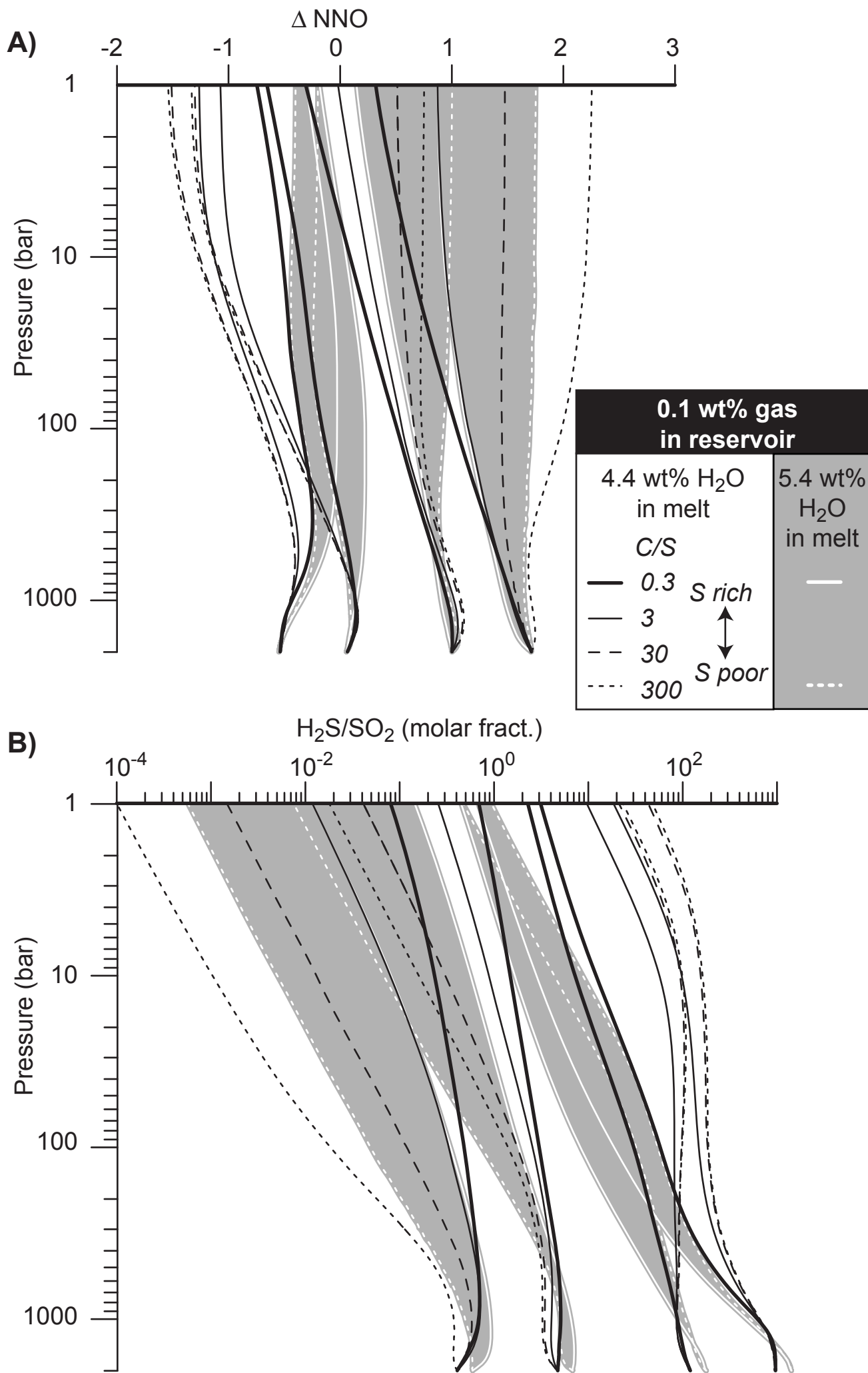


Figure 3

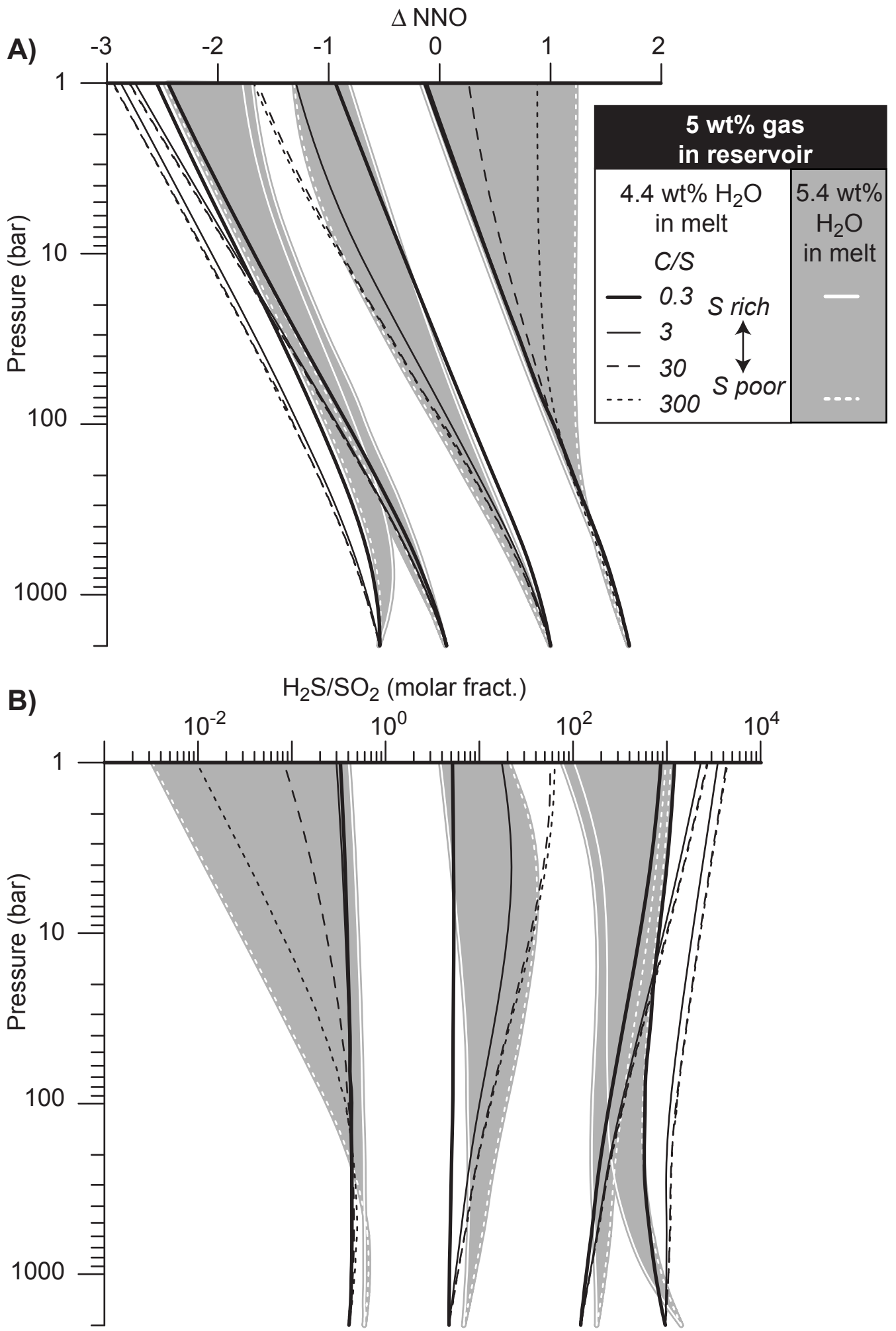


Figure 4

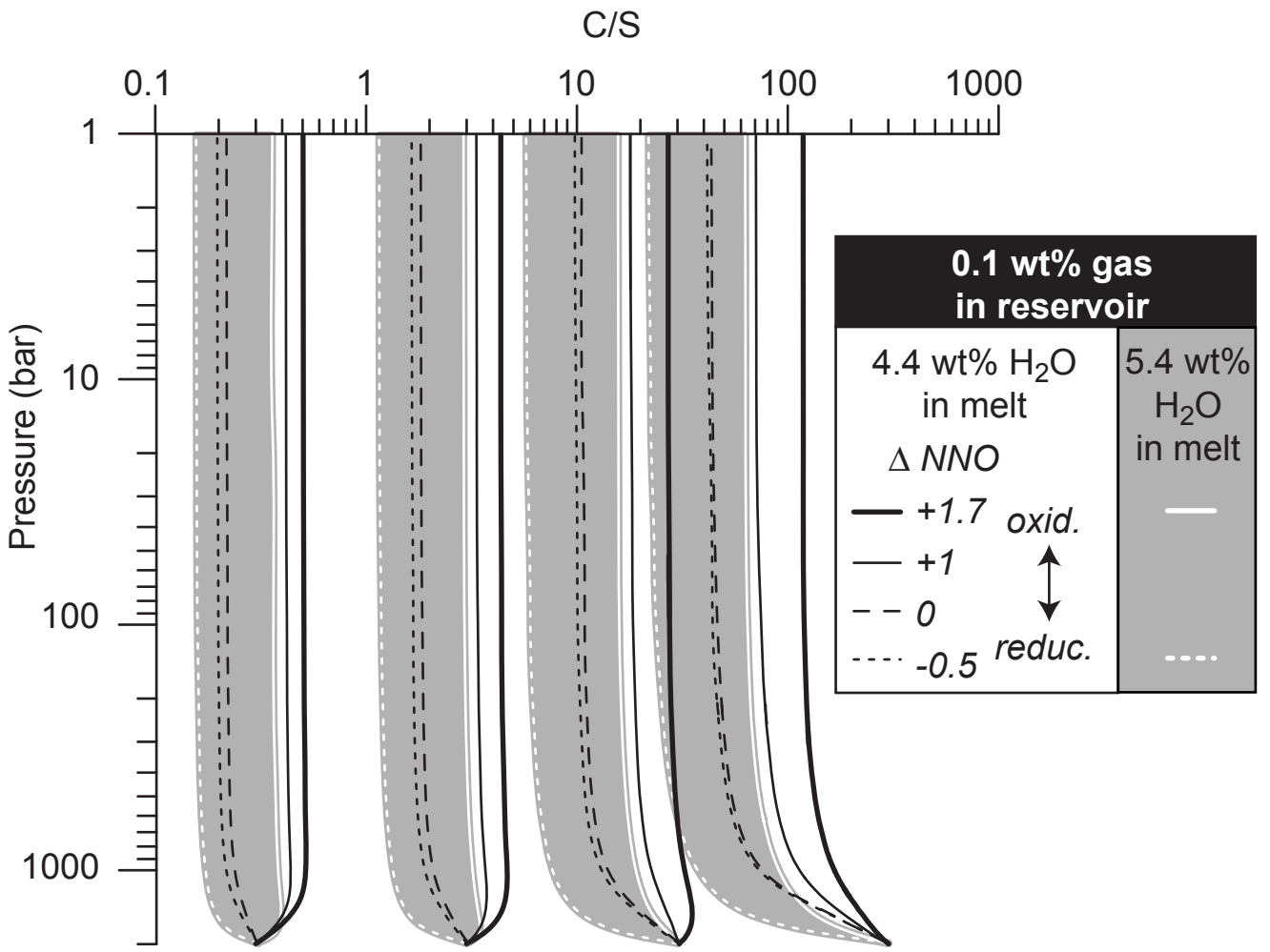


Figure 5

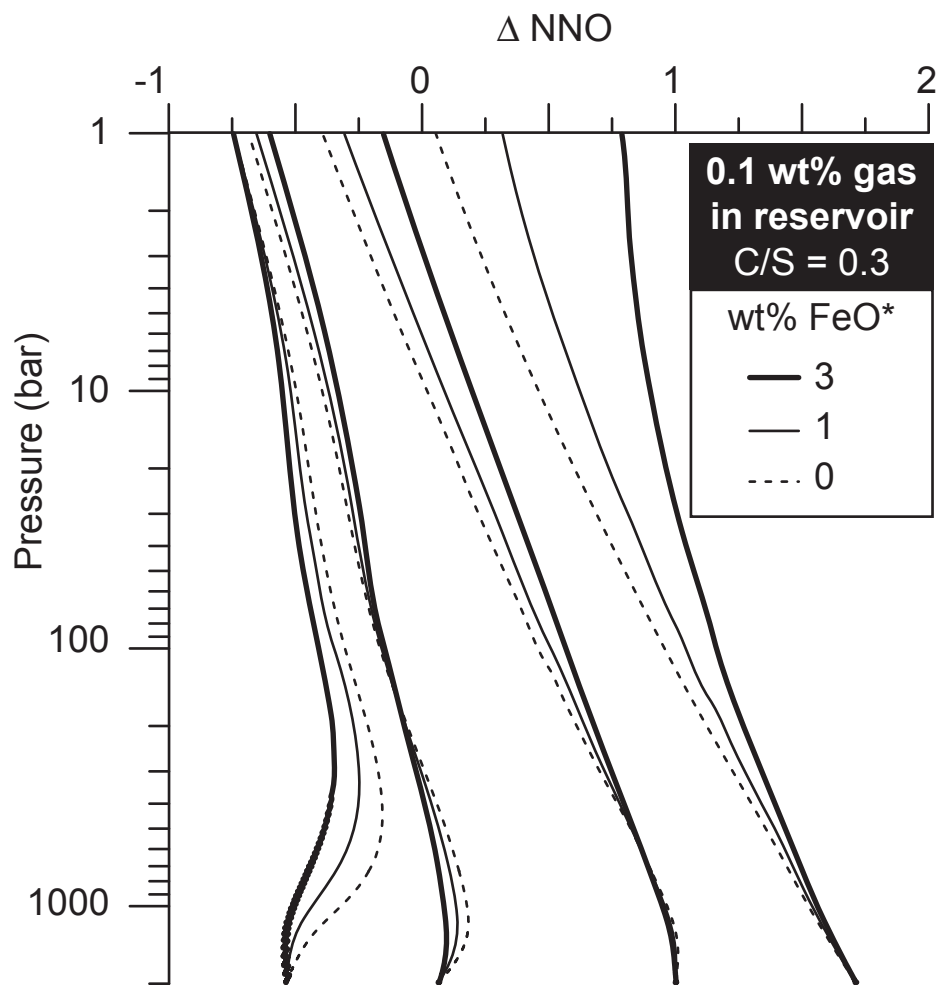


Figure 6

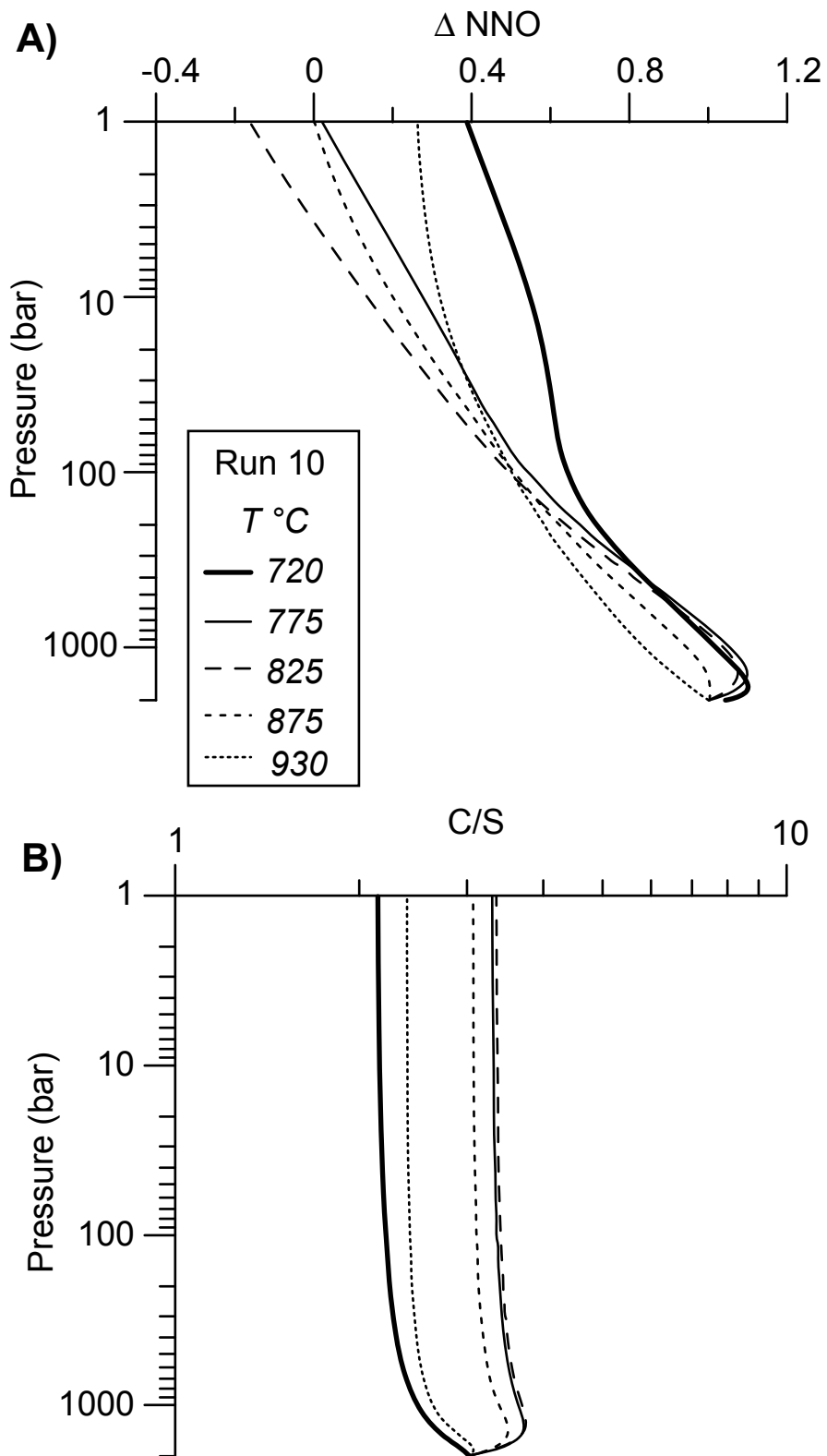


Figure 7

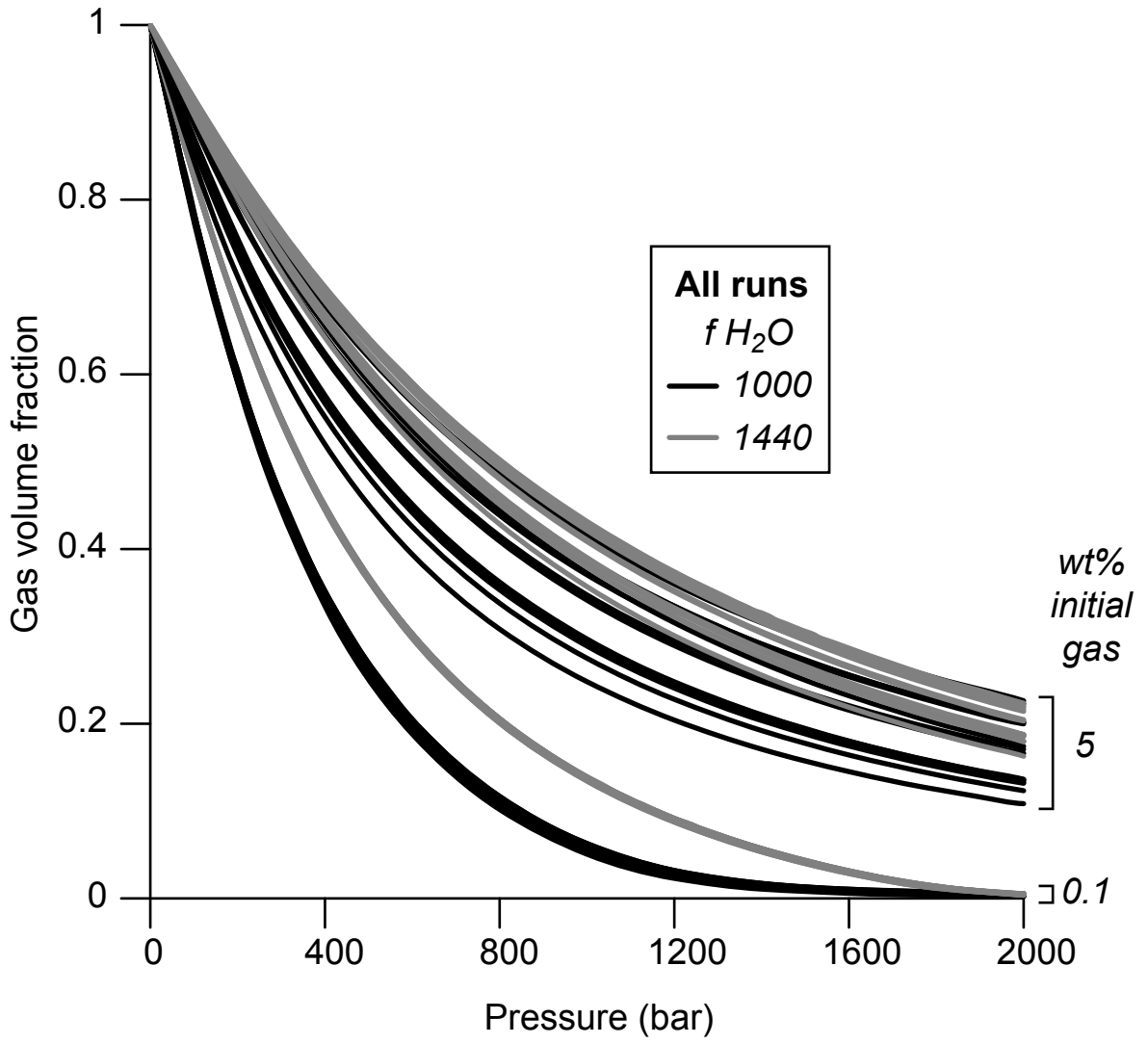


Figure 8

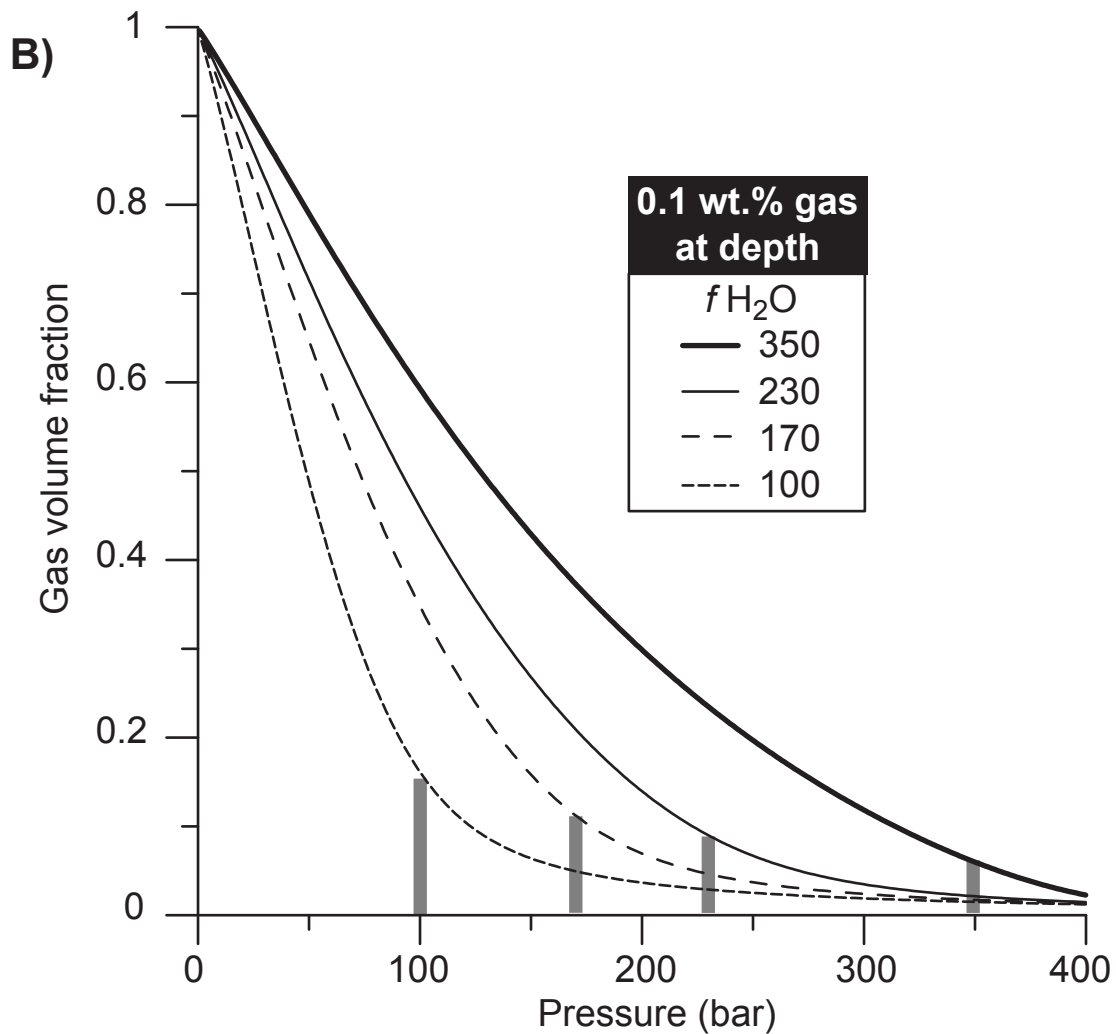
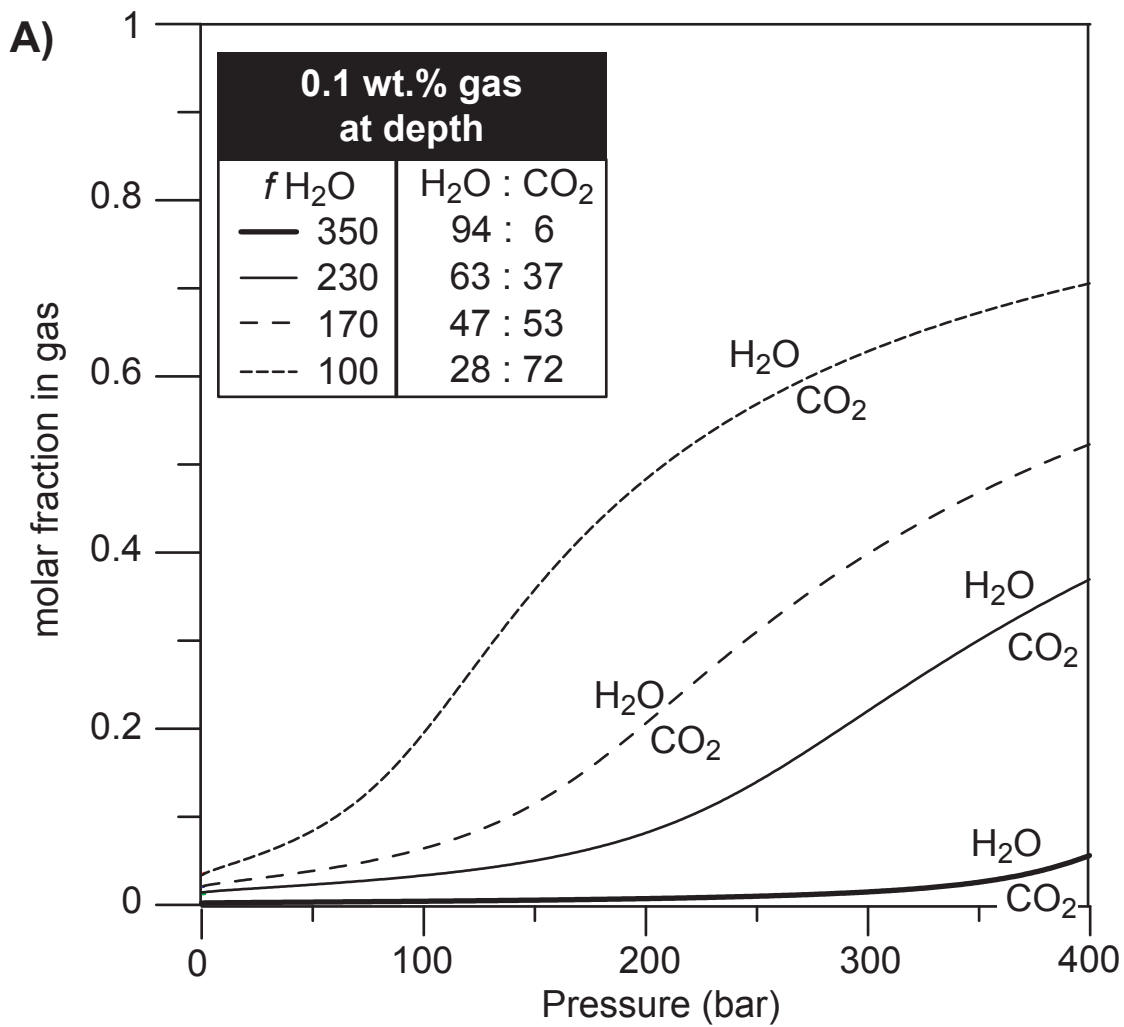


Figure 9

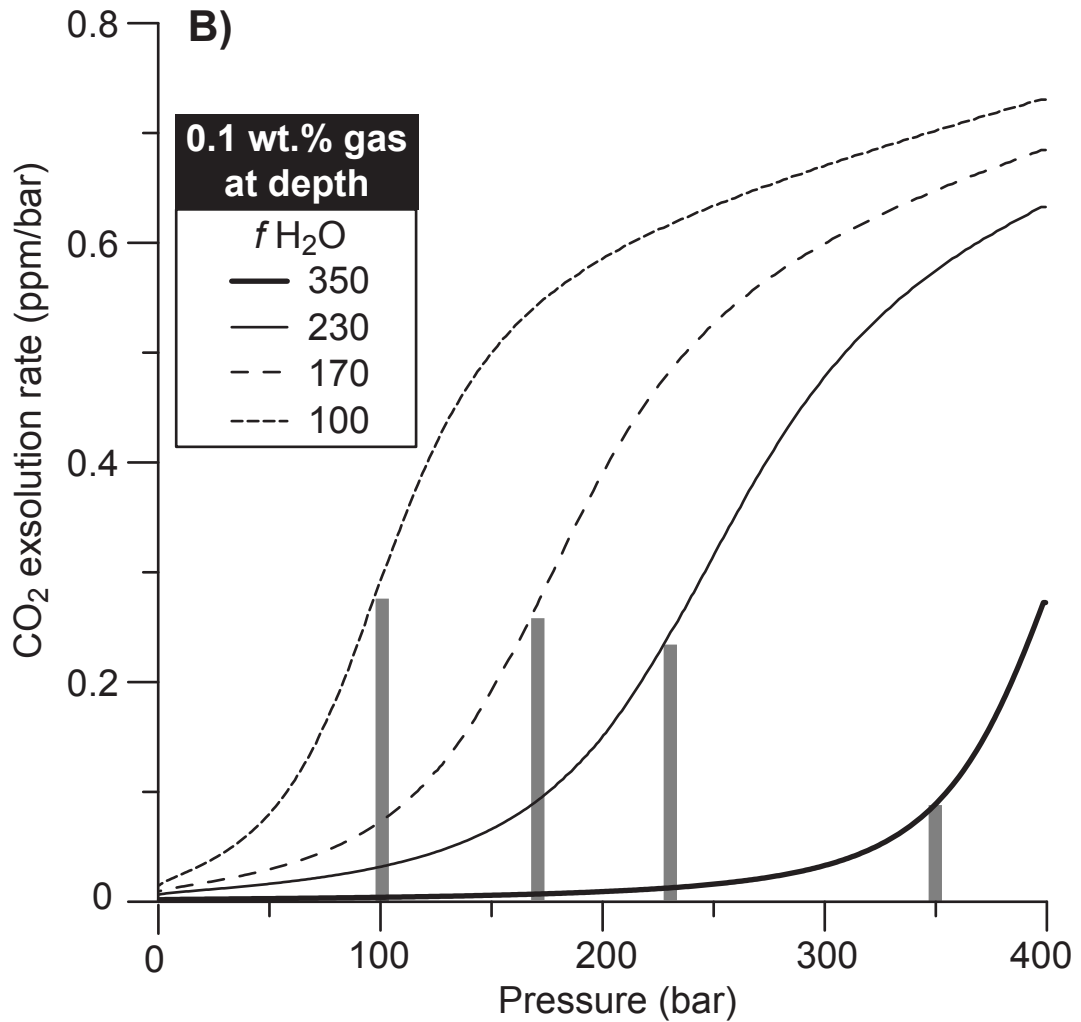
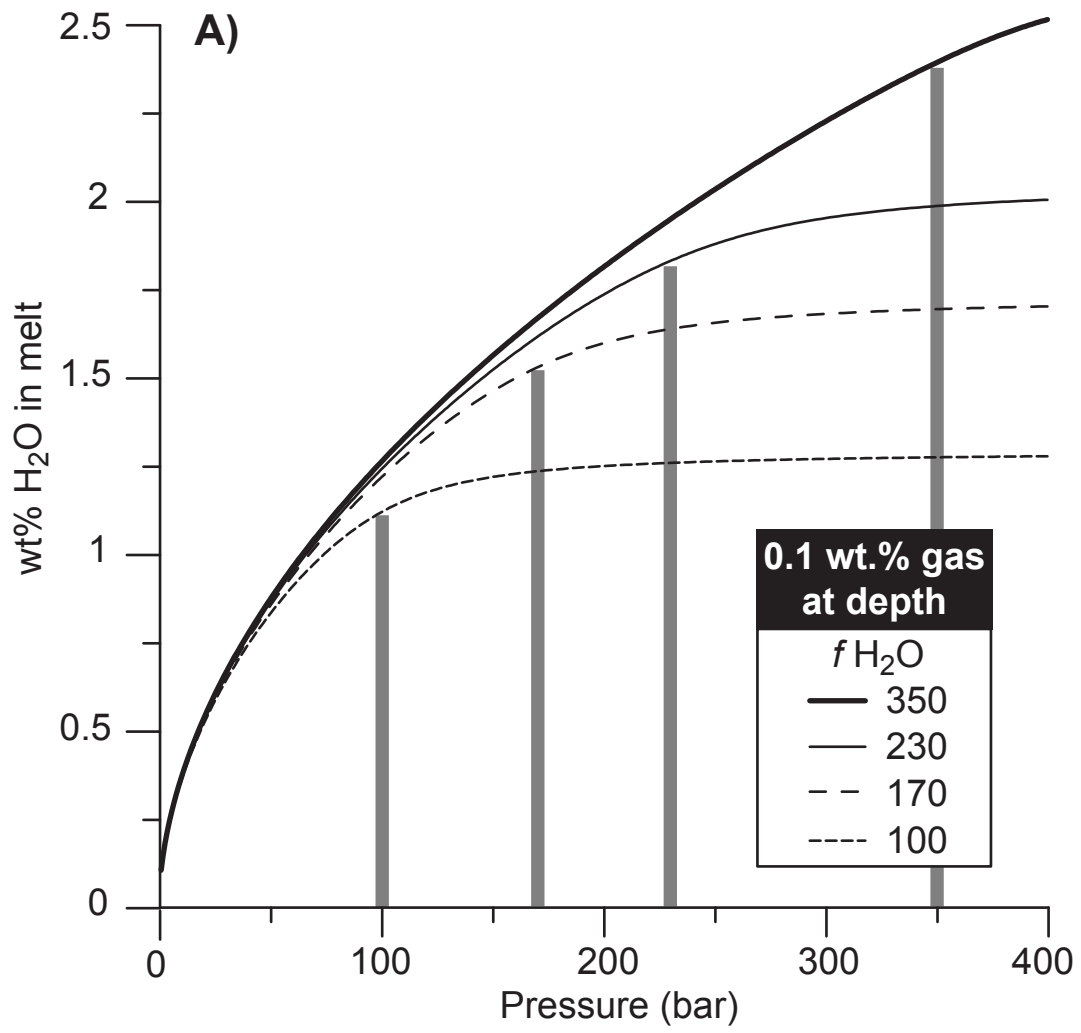


Figure 10

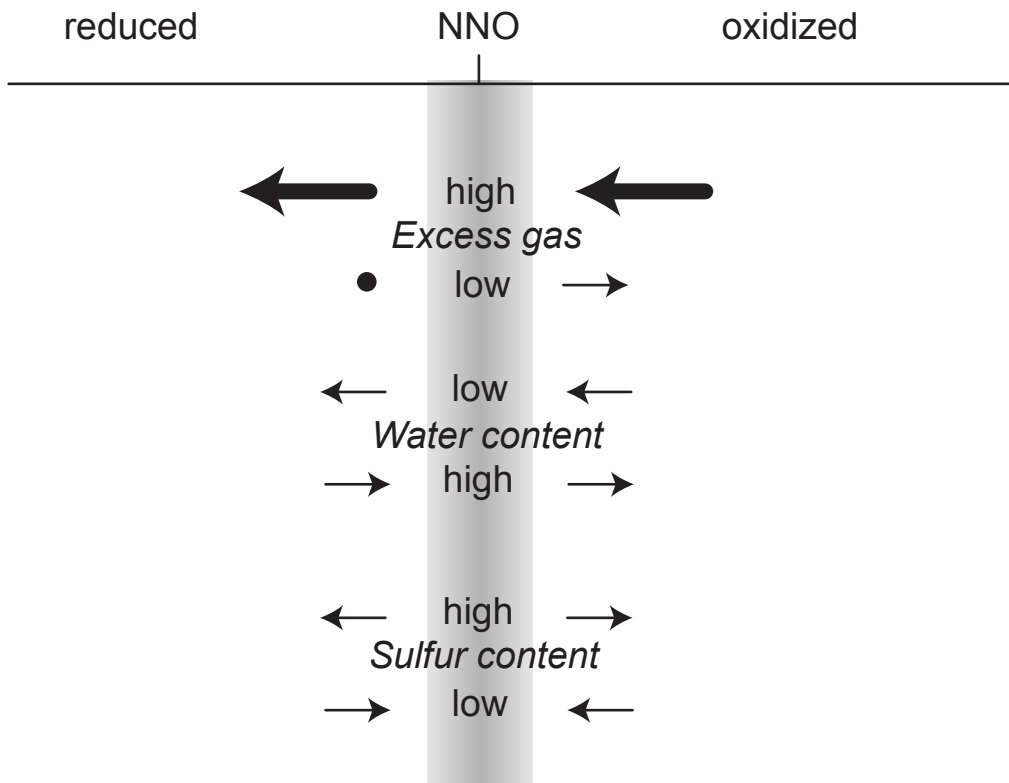


Figure 11

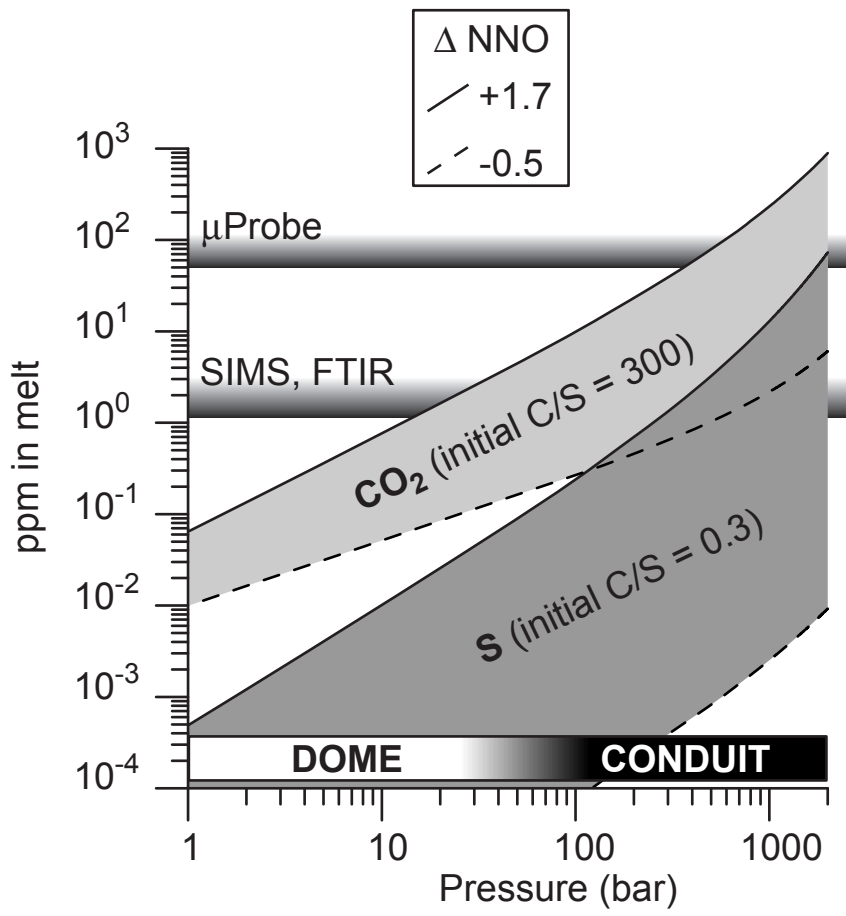


Figure 12

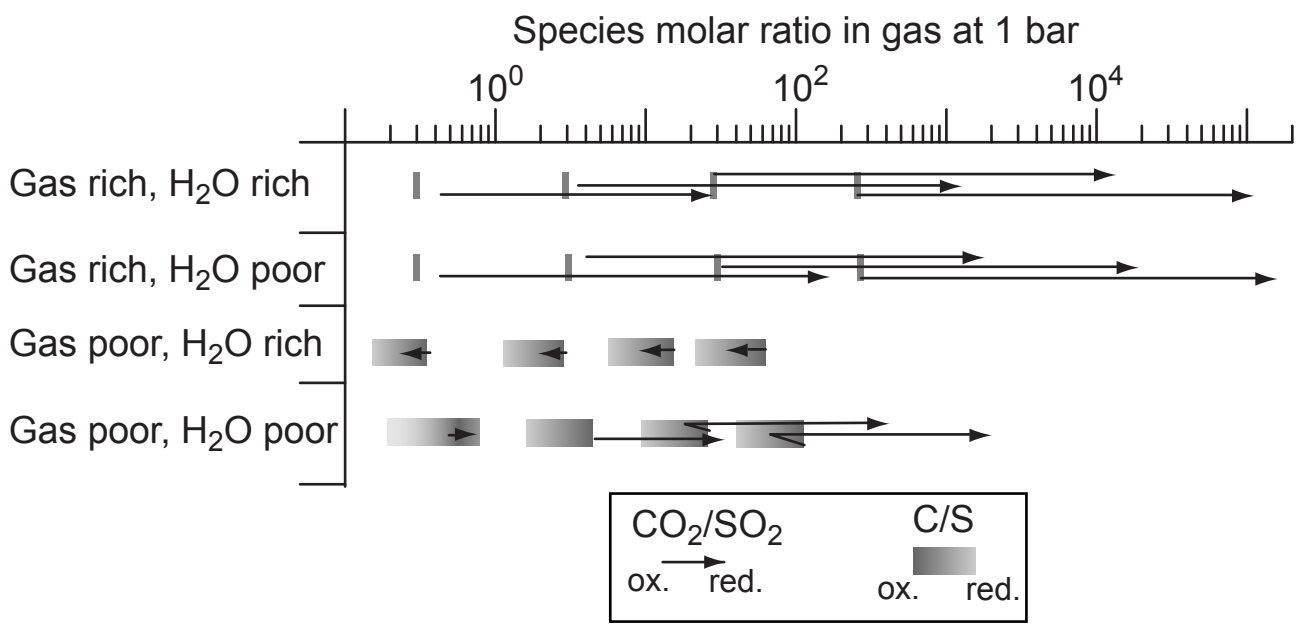


FIGURE 13